J. Fluid Mech. (2020), *vol.* 885, A25. © Cambridge University Press 2019
doi:10.1017/jfm.2019.994

Start-up flow in shallow deformable microchannels

Alejandro Martínez-Calvo[1,†], Alejandro Sevilla[1], Gunnar G. Peng[2] and Howard A. Stone[3]

[1]Grupo de Mecánica de Fluidos, Departamento de Ingeniería Térmica y de Fluidos, Universidad Carlos III de Madrid, Av. Universidad 30, 28911 Leganés (Madrid), Spain

[2]Department of Applied Mathematics and Theoretical Physics, University of Cambridge, Wilberforce Road, Cambridge CB3 0WA, UK

[3]Department of Mechanical and Aerospace Engineering, Princeton University, Princeton, NJ 08544, USA

(Received 19 February 2019; revised 2 October 2019; accepted 24 November 2019)

Microfluidic systems are usually fabricated with soft materials that deform due to the fluid stresses. Recent experimental and theoretical studies on the steady flow in shallow deformable microchannels have shown that the flow rate is a nonlinear function of the pressure drop due to the deformation of the upper soft wall. Here, we extend the steady theory of Christov *et al.* (*J. Fluid Mech.*, vol. 841, 2018, pp. 267–286) by considering the start-up flow from rest, both in pressure-controlled and in flow-rate-controlled configurations. The characteristic scales and relevant parameters governing the transient flow are first identified, followed by the development of an unsteady lubrication theory assuming that the inertia of the fluid is negligible, and that the upper wall can be modelled as an elastic plate under pure bending satisfying the Kirchhoff–Love equation. The model is governed by two non-geometrical dimensionless numbers: a compliance parameter β, which compares the characteristic displacement of the upper wall with the undeformed channel height, and a parameter γ that compares the inertia of the solid with its flexural rigidity. In the limit of negligible solid inertia, $\gamma \to 0$, a quasi-steady model is developed, whereby the fluid pressure satisfies a nonlinear diffusion equation, with β as the only parameter, which admits a self-similar solution under pressure-controlled conditions. This simplified lubrication description is validated with coupled three-dimensional numerical simulations of the Navier equations for the elastic solid and the Navier–Stokes equations for the fluid. The agreement is very good when the hypotheses behind the model are satisfied. Unexpectedly, we find fair agreement even in cases where the solid and liquid inertia cannot be neglected.

Key words: microfluidics, lubrication theory

1. Introduction

Microfluidic devices allow the manipulation of fluids and objects inside channels whose typical dimensions vary from tens to hundreds of microns. These systems have

† Email address for correspondence: amcalvo@ing.uc3m.es

https://doi.org/10.1017/jfm.2019.994 Published online by Cambridge University Press

drastically reduced the working space and the time involved in the applications where they are used. In particular, these devices are routinely used to control multiphase flows, e.g. to generate monodisperse bubbles and droplets, to manipulate immersed soft and hard objects, namely particles, capsules, cells or vesicles, or in diverse applications such as sorting, mixing, drug delivery or mass spectroscopy. The development of microfluidics has facilitated a myriad of applications in a large variety of fields, both in scientific and engineering contexts, e.g. biology (El-Ali, Sorger & Jensen 2006), pharmacy and medicine (Rodríguez-Rodríguez *et al.* 2015) or biomedical research (Sackmann, Fulton & Beebe 2014). For more detailed information the reader is referred to the reviews of Stone, Stroock & Ajdari (2004), Tabeling (2005), Squires & Quake (2005), Whitesides (2006), Bruus (2008) and Anna (2016).

The development of soft lithography (Xia & Whitesides 1998) played a crucial role in reducing the manufacturing cost and time of these microfluidic platforms. Soft lithography implies the use of highly flexible materials like polydimethylsiloxane (PDMS), since it is cheap, biocompatible, has a low curing time and is transparent, which facilitates experimental measurements. These materials are cured on a harder substrate, typically glass, which does not deform appreciably under the characteristic overpressures achieved within the channel, in contrast with the PDMS walls, which may experience a substantial deformation. Hence, the use of soft materials in microfluidics naturally gives rise to coupled fluid–structure interaction (FSI) problems under flow (Squires & Quake 2005; Bruus 2008; Duprat & Stone 2016). In fact, many applications take advantage of the deformation of the compliant walls, whose passive or active control allows the development of soft actuators in lab-on-a-chip devices, e.g. valves, pumps, self-regulating components or flow rectifiers, and has also facilitated the development of soft robotics (Ilievski *et al.* 2011; Shepherd *et al.* 2011; Elbaz & Gat 2014; Majidi 2014; Rus & Tolley 2015; Polygerinos *et al.* 2017).

Traditionally, FSI problems have been studied in the context of high-Reynolds-number flows relevant to civil, aeronautical and naval engineering, where aeroelastic and hydroelastic couplings play a crucial role (Païdoussis, Price & De Langre 2010; Bisplinghoff, Ashley & Halfman 2013). In the last few decades, there is a growing attention to FSI problems at small scales due to their ubiquity in nature and in many engineering applications beyond microfluidics. Such is the case of elastocapillarity (Bico, Reyssat & Roman 2018), peeling processes (Juel, Pihler-Puzović & Heil 2018), the flow around swimming bacterial colonies (Lauga 2016) or around vesicles and blood cells in compliant capillaries (Goldsmith & Skalak 1975; Secomb, Hsu & Pries 2002), where FSI is crucial to understanding the underlying physics. A particularly important context where small-scale FSI problems arise is in biological flows (Fung 1993*a*,*b*,*c*), e.g. in the pulmonary and respiratory systems (Grotberg 1994, 2001; Grotberg & Jensen 2004; Heil & Hazel 2011). Within this context, a large amount of work has been done to understand the dynamics of fluid-filled elastic tubes that may collapse and buckle due to the transmural pressure (Conrad 1969; Shapiro 1977; Cancelli & Pedley 1985; Pedley & Luo 1998; Heil *et al.* 2003). Although most of these studies deal with finite Reynolds numbers, there are also some works dealing with Stokes flow and lubrication theory in this configuration (Heil & Pedley 1995; Heil 1997). Furthermore, there are still important open problems concerning haemodynamics in vascular networks, involving vascular remodelling, regulation of blood flow, oxygen transport, the fluid pressure distribution or the shear stress exerted at the compliant vessel walls, which are crucial in the development and detection of cardiovascular diseases such as aneurysms or ischaemias, or even in tumour angiogenesis (Goldsmith & Skalak 1975; Pedley 1980; Taylor & Draney 2004; Popel & Johnson 2005; Cassot *et al.* 2006; Lasheras 2007; Sforza, Putman & Cebral 2009).

https://doi.org/10.1017/jfm.2019.994 Published online by Cambridge University Press

In the present work we focus on the incompressible start-up flow in a shallow microchannel of rectangular cross-section that is filled with a Newtonian liquid, and whose upper soft wall deforms due to the overpressure needed to induce the flow. It is well known that in the low-Reynolds-number flow of liquids inside rigid channels of constant cross-section, the flow rate q is proportional to the pressure drop Δp. The constant of proportionality is usually referred to as the hydraulic resistance, which only depends on the geometry of the cross-section, on the channel length and on the fluid dynamic viscosity (Happel & Brenner 2012). However, several authors have shown through experiments, theory and simulations that the relationship between q and Δp is nonlinear when the deformation of the walls induced by the fluid pressure is not negligible (Gervais *et al.* 2006; Hardy *et al.* 2009; Seker *et al.* 2009; Cheung, Toda-Peters & Shen 2012; Ozsun, Yakhot & Ekinci 2013; Raj & Sen 2016; Raj, DasGupta & Chakraborty 2017; Christov *et al.* 2018). Under steady flow conditions, these authors found that, for a given imposed pressure drop, the flow rate is larger than that associated with the corresponding rigid channel. Indeed, higher throughputs can be achieved in deformable microchannels due to a decrease in the hydraulic resistance induced by the wall compliance.

The steady lubrication theory developed by Christov *et al.* (2018) assumes that only the upper wall is deformable. Note that, in most microchannels, the bottom wall is rigid, but the lateral ones are made of the same soft material as the upper one, and thus may also deform. Nevertheless, in shallow geometries the deformation of the lateral walls has a negligible effect outside thin lateral elastic boundary layers, as evidenced by the scaling analysis of Gervais *et al.* (2006). In addition, the thickness of the lateral walls is typically much larger than the thickness of the upper wall, in which case the lateral wall deformation is much smaller than the upper one. Christov *et al.* (2018) described the upper wall as a plate under pure bending modelled with the linear Kirchhoff–Love theory (Love 1888). Previous studies (cf. Gervais *et al.* 2006; Hardy *et al.* 2009; Raj & Sen 2016; Raj *et al.* 2017) considered a global Hookean relation between the fluid pressure and the spanwise average of the upper wall's vertical displacement, thus neglecting spanwise bending and considering that the displacement profile is a quadratic function of the spanwise coordinate, instead of the quartic profile predicted by the Kirchhoff–Love plate theory. Introducing the hypothesised Hookean relation into the standard q–Δp function, these authors deduced a model with one fitting parameter that absorbs the geometric and material constants. This model was able to explain the trends observed in the experiments of Gervais *et al.* (2006) with thick-walled microchannels. However, Christov *et al.* (2018) showed that this approximation fails in many configurations, e.g. when the thickness of the top wall is smaller than or comparable to the channel's width. In contrast, the lubrication theory of Christov *et al.* (2018) does not have any fitting parameter, and depends only on a compliance parameter $\tilde{\beta}$, that arises naturally from the coupling between the steady fluid flow, described with lubrication theory, and the upper wall displacement, described with the Kirchhoff–Love plate theory. The parameter $\tilde{\beta}$ compares the characteristic displacement of the upper wall with its undeformed height or, equivalently, the characteristic overpressure with the flexural rigidity of the upper wall. Christov *et al.* (2018) also made direct comparisons of their theory with the experimental data of Ozsun *et al.* (2013), finding good agreement without fitting parameters. More recently, Shidhore & Christov (2018) have extended these ideas deriving a lubrication model for microchannels with a thicker top wall, whose displacement is modelled with the Mindlin theory accounting for shear stresses. They also performed steady three-dimensional (3-D) numerical simulations for both

https://doi.org/10.1017/jfm.2019.994 Published online by Cambridge University Press

thin and thick upper walls, finding good agreement with their lubrication models, but worse agreement with the experimental data of Ozsun *et al.* (2013). Gervais *et al.* (2006) also conducted 3-D numerical simulations of the steady flow. However, they did not apply clamped boundary conditions for the top wall displacement at the inlet and outlet of the microchannel, and they did not impose the exact continuity of stresses at the fluid–solid interface.

All the studies mentioned in the previous paragraph focused on steady flow. There are also two previous experimental and theoretical works dealing with unsteady flow in deformable microchannels, namely Dendukuri *et al.* (2007) and Panda *et al.* (2009). In particular, both studies considered the stop flow associated with the relaxation of a top wall initially deflected by the fluid stresses, which induces a squeeze flow towards the inlet and the outlet of the microchannel. To derive their lubrication models, these authors neglected the solid and the liquid inertia, and obtained a nonlinear diffusion equation for the vertical displacement of the upper wall. However, the latter equation is markedly different from the one developed herein, since it is based on a Hookean relation between the vertical displacement of the upper wall and the fluid pressure neglecting spanwise bending, which is valid in the limit of a very thick wall, but not in the case of a thin plate. In particular, Dendukuri *et al.* (2007) determined the relaxation time of the upper wall through scaling arguments, finding good agreement with their own experiments with one fitting parameter, equivalent to that introduced by Gervais *et al.* (2006) in the case of steady flow. In the present work, we show that the model developed by Dendukuri *et al.* (2007), although an important step forward, fails to describe the unsteady flow for most geometries and wall materials. Another important contribution of Dendukuri *et al.* (2007) was to show that the characteristic time scale only depends on the geometry of the channel and on the fluid and solid properties, but not on the fluid pressure or flow rate, in agreement with the results developed herein. The lubrication model of Dendukuri *et al.* (2007) was solved numerically by Panda *et al.* (2009), and compared with stop-flow experiments performed with thick-walled microchannels. The main limitations of the unsteady lubrication theory developed by Dendukuri *et al.* (2007) are the same as those of the steady lubrication model of Gervais *et al.* (2006), whose shortcomings were indicated by Christov *et al.* (2018).

An unsteady analysis similar to the one presented herein was performed by Elbaz & Gat (2014) for a thin cylindrical soft shell conveying a viscous fluid. These authors identified the characteristic time scale of the unsteady flow, which is equivalent to the one deduced in the present work. In addition, they developed an unsteady lubrication theory neglecting liquid and solid inertia, and deduced a diffusion equation for the fluid pressure. However, the latter equation is linear, since only small values of the compliance parameter, corresponding to small deformations, were considered by Elbaz & Gat (2014). Furthermore, Elbaz & Gat (2016) extended the latter work to account for the transient viscous flow within an annular gap between a rigid shaft and a concentric elastic tube. Using an elasto-hydrodynamic lubrication approximation, they also deduced self-similar solutions of the propagation front for small and large prewetting thickness compared to the radial displacement, neglecting streamwise bending and shear stresses. Asymptotic solutions including bending and tension close to the peeling front were also obtained in the latter work. More recently, Elbaz, Jacob & Gat (2018) studied the unsteady viscous flow of a gas within a two-dimensional narrow gap, by means of the lubrication approximation.

In the present work, we extend the steady theory of Christov *et al.* (2018) to account for transient flow, and apply the new framework to the canonical problem of

https://doi.org/10.1017/jfm.2019.994 Published online by Cambridge University Press

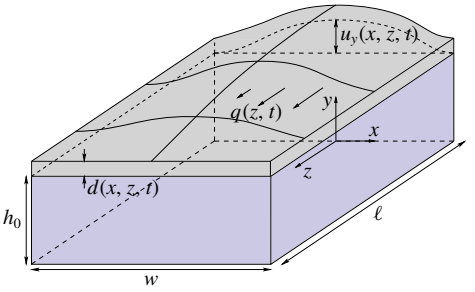


FIGURE 1. Sketch of the flow configuration.

start-up flow from rest. From the theoretical point of view, our main motivation is to provide a framework to tackle FSI problems in laminar internal flows dominated by viscous forces. Indeed, although only the start-up flow is analysed herein for brevity, a similar formalism can be developed to study other transient problems such as stop flows or oscillatory flows. Additional motivation comes from a basic question that, to the best of our knowledge, remains unanswered: What is the start-up time of the flow in a deformable microchannel, and how does it depend on the liquid and solid properties? To that end, we first identify the characteristic hydro-elastic scales and the relevant parameters governing the unsteady flow. Then we develop an unsteady lubrication theory accounting for the solid and liquid inertia, assuming that the upper wall is governed by the Kirchhoff–Love theory in the bending-dominated regime. When the liquid and solid inertia are negligible, we derive a nonlinear diffusion equation for the fluid pressure field. To check the model, we perform 3-D direct numerical simulations of the Navier and Navier–Stokes equations for the solid and for the liquid respectively, and compare the results with the quasi-steady lubrication model.

The paper is organised as follows: the flow configuration is described in § 2. The mathematical formulation is presented in § 3 making use of the Navier and Navier–Stokes equations for the elastic upper wall and the incompressible flow, respectively. In § 4 we identify the characteristic scales and the dimensionless parameters governing the flow, and we develop an unsteady lubrication theory for the elasto-hydrodynamic problem, which is further simplified in the quasi-steady limit of negligible liquid and solid inertia. The results are presented in § 5, including a comparison between the quasi-steady lubrication model and the 3-D numerical simulations. Conclusions are drawn in § 6.

2. Flow configuration

As sketched in figure 1, we consider the incompressible start-up flow in a channel of length ℓ, width w and height h, where $h \ll w \ll \ell$, initially filled with a Newtonian fluid of density ρ and dynamic viscosity μ. The overpressure needed to convey the fluid deforms the soft walls, which in turn affects the hydraulic resistance of the channel, giving rise to a coupled fluid–structure problem (Gervais *et al.* 2006; Weibel *et al.* 2007; Hardy *et al.* 2009; Ozsun *et al.* 2013). Assuming that only the upper wall deforms, here we extend the results of Christov *et al.* (2018) to unsteady flow.

We adopt a Cartesian coordinate system (x, y, z) as shown in figure 1, and use $\boldsymbol{v} = (v_x, v_y, v_z)$ to denote the fluid velocity field and $\boldsymbol{u} = (u_x, u_y, u_z)$ to denote the

https://doi.org/10.1017/jfm.2019.994 Published online by Cambridge University Press

displacement field of the upper wall, of thickness $d(x, z, t)$. We also use $u_y(x, z, t)$ to denote the vertical displacement of the lower surface of the upper wall, i.e. the fluid–solid boundary, so that its position is given by

$$y = h(x, z, t) = h_0 + u_y(x, z, t), \tag{2.1}$$

where h_0 is the undeformed height of the channel. The displacement is induced by the fluid pressure $p(x, y, z, t)$, which is measured with respect to the outer atmospheric pressure. The flow rate $q(z, t)$ in the z-direction is given by the cross-sectional integral of the axial velocity v_z as

$$q(z, t) = \int_{-w/2}^{w/2} \int_0^{h(x,z,t)} v_z(x, y, z, t)\, \mathrm{d}y\, \mathrm{d}x. \tag{2.2}$$

For times $t < 0$, the fluid is at rest with $p = 0$ and $\boldsymbol{v} = \boldsymbol{0}$, and thus the solid remains undeformed, $\boldsymbol{u} = \boldsymbol{0}$. For $t > 0$, a start-up flow takes place, either due to an imposed inlet flow rate $q(z = 0, t) = q_0$ (flow-rate-controlled situation) or due to an imposed inlet overpressure $p(z = 0, t) = \Delta p > 0$ (pressure-controlled situation). We assume that the outlet pressure is $p(z = \ell, t) = 0$.

To address the start-up flow we have developed two techniques, namely: (i) 3-D numerical simulations of the full Navier–Stokes equations for the flow field and the Navier equations for the solid deformation field, contemplating both linear and nonlinear strains; and (ii) a lubrication theory assuming that the upper wall behaves according to the linear Kirchhoff–Love equation for a plate under pure bending (Love 1888), neglecting changes in its thickness, d.

3. Formulation of the problem

Although the main objective of the present study is to develop an unsteady lubrication theory to describe the start-up flow (see § 4), to check its validity we have also performed 3-D direct numerical simulations of the Navier equations for a linear elastic upper wall of finite thickness, fully coupled to the Navier–Stokes equations for the incompressible flow of a Newtonian liquid. The fluid velocity field is governed by the continuity and momentum equations

$$\boldsymbol{\nabla} \cdot \boldsymbol{v} = 0 \quad \text{and} \quad \rho(\partial_t \boldsymbol{v} + \boldsymbol{v} \cdot \boldsymbol{\nabla} \boldsymbol{v}) = \boldsymbol{\nabla} \cdot \boldsymbol{T}, \tag{3.1a,b}$$

where $\boldsymbol{T} = -p\boldsymbol{I} + \mu(\boldsymbol{\nabla} \boldsymbol{v} + \boldsymbol{\nabla} \boldsymbol{v}^{\mathrm{T}})$ is the fluid stress tensor. The fluid velocity field must satisfy the no-slip conditions at the rigid walls

$$\boldsymbol{v} = \boldsymbol{0} \quad \text{at } y = 0, \quad \text{and} \quad x = \pm w/2, \tag{3.2a,b}$$

and atmospheric conditions at the outlet

$$p = 0 \quad \text{and} \quad \boldsymbol{T} \cdot \boldsymbol{e}_z = \boldsymbol{0} \quad \text{at } z = \ell. \tag{3.3a,b}$$

At the inlet, we either impose a fixed pressure Δp and no shear stress,

$$p = \Delta p \quad \text{and} \quad \boldsymbol{T} \cdot \boldsymbol{e}_z = \boldsymbol{0} \quad \text{at } z = 0 \ (\textit{pressure-controlled}), \tag{3.4a,b}$$

or a given axial flow profile $v_0(x, y)$ corresponding to an input flow rate $q = q_0$ (see appendix B) satisfying no slip conditions

$$v_z = v_0(x, y) \quad \text{and} \quad v_x = v_y = 0 \quad \text{at } z = 0 \ (\textit{flow-rate-controlled}). \tag{3.5a,b}$$

https://doi.org/10.1017/jfm.2019.994 Published online by Cambridge University Press

At the contact surface between the liquid and the soft wall, the continuity of velocities must hold,

$$\boldsymbol{v} = \partial_t \boldsymbol{u} \quad \text{at } y = h(x, z, t). \tag{3.6}$$

The elastic upper wall satisfies the Cauchy equation of motion under the small-displacement approximation

$$\rho_s \partial_t^2 \boldsymbol{u} = \boldsymbol{\nabla} \cdot \boldsymbol{\sigma}, \tag{3.7}$$

where ρ_s is the upper wall material density, $\boldsymbol{\sigma} = 2\mu_s \boldsymbol{\varepsilon} + \lambda_s \mathrm{tr}(\boldsymbol{\varepsilon})\boldsymbol{I}$ is the solid stress tensor of a so-called Hookean elastic material, $\boldsymbol{\varepsilon}$ is the strain tensor and $\mu_s = E/[2(1+\nu)]$ and $\lambda_s = E\nu/[(1+\nu)(1-2\nu)]$ are the two Lamé constants, expressed in terms of the Young modulus E and Poisson ratio ν. The main results of § 5 have been obtained assuming that the strain is linear in the displacement gradients

$$\boldsymbol{\varepsilon} = \tfrac{1}{2}(\boldsymbol{\nabla u} + \boldsymbol{\nabla u}^{\mathrm{T}}), \tag{3.8}$$

which is a good approximation whenever $|\partial_j u_i| \ll 1$ for all i and j. But we have also used the complete nonlinear expression of the strain tensor,

$$\boldsymbol{\varepsilon} = \tfrac{1}{2}(\boldsymbol{\nabla u} + \boldsymbol{\nabla u}^{\mathrm{T}} + \boldsymbol{\nabla u} \cdot \boldsymbol{\nabla u}^{\mathrm{T}}), \tag{3.9}$$

to check whether stretching of the wall has a significant effect. This nonlinear stretching may be significant even when the strain $\boldsymbol{\varepsilon}$ is small and the linear stress–strain relationship holds, such as for a thin elastic sheet that is deflected by an amount u_y comparable to or larger than its thickness d, which can be modelled using the Föppl–von Kármán equations.

The lateral walls of the solid are clamped, so that $\boldsymbol{u}$ satisfies

$$\boldsymbol{u} = \boldsymbol{0} \quad \text{at } z = 0, z = \ell, \quad \text{and} \quad x = \pm w/2. \tag{3.10a,b}$$

At the fluid–solid interface the continuity of stresses must be fulfilled,

$$(\boldsymbol{\sigma} + \boldsymbol{T}) \cdot \boldsymbol{n} = \boldsymbol{0} \quad \text{at } y = h(x, z, t), \tag{3.11}$$

where $\boldsymbol{n}$ is the unit normal vector to the liquid–solid interface. Finally, we impose a stress-free condition at the upper surface of the top wall,

$$\boldsymbol{\sigma} \cdot \boldsymbol{n}_{ext} = \boldsymbol{0} \quad \text{at } y = h(x, z, t) + d(x, z, t), \tag{3.12}$$

where $\boldsymbol{n}_{ext}$ is the unit normal vector to the upper surface of the soft wall. To perform 3-D numerical simulations, the complete system of (3.1)–(3.12) is expressed in weak form and solved with the finite-element software COMSOL Multiphysics employing the arbitrary Lagrangian–Eulerian (ALE) method. The details of the numerical techniques employed herein are provided in appendix B.

Figure 2(*a*) shows a first comparison of the two calculational frameworks employed herein under steady-state conditions, namely 3-D numerical simulations and lubrication theory (Christov *et al.* 2018). In particular, the results show the pressure drop along the channel Δp as a function of the flow rate q, which is also used as a validation of the numerical method by comparing with the S4 experiment of Ozsun *et al.* (2013). These experiments were performed in a PDMS microchannel with water as a working liquid, and whose relevant physical parameters are given in table 2. Our 3-D numerical simulations (blue triangles) are in excellent agreement with the experiments (circles), whereas the lubrication approximation (blue solid line) properly captures the nonlinear

https://doi.org/10.1017/jfm.2019.994 Published online by Cambridge University Press

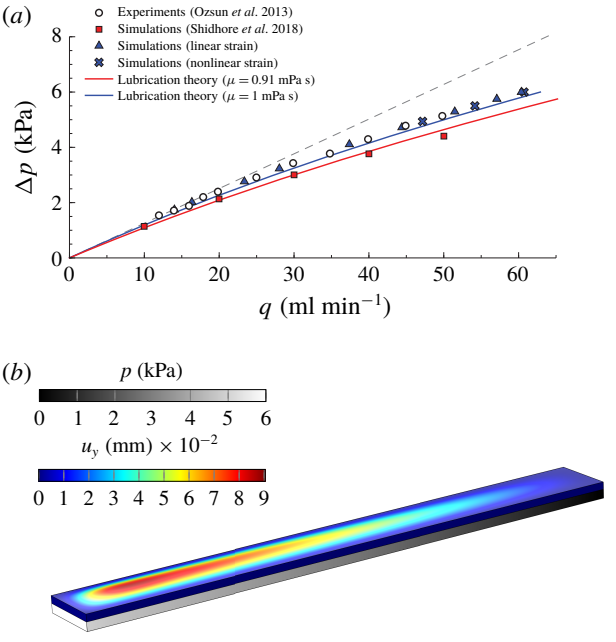


FIGURE 2. (*a*) Pressure drop as a function of flow rate extracted from the S4 experiments of Ozsun *et al.* (2013) (circles), the numerical simulations of Shidhore & Christov (2018) with $\mu = 0.91$ mPa s (red squares), the present numerical simulations considering $\mu =$ 1 mPa s with either a linear strain (3.8) (blue triangles) or a nonlinear strain (3.9) (blue crosses), and the corresponding lubrication theory of Christov *et al.* (2018) for both values of the viscosity (solid lines). The dashed line represents the lubrication solution for rigid channels. (*b*) Steady 3-D numerical simulation of the S4 system of Ozsun *et al.* (2013) for an imposed inlet pressure of $\Delta p = 6$ kPa, showing the liquid pressure p and the vertical solid displacement u_y. All the results have been computed for the geometry described in table 2 using water as working liquid (case II).

trend, but slightly overestimates the flow rate, as already shown by Christov *et al.* (2018). The numerical simulations of Shidhore & Christov (2018) are also shown (red squares), although they were carried out taking a liquid viscosity of $\mu = 0.91$ mPa s, which corresponds to a room temperature of approximately 24 °C, whereas ours were computed for $\mu = 1$ mPa s, corresponding to a room temperature of 20 °C (see case II in table 2). The prediction according to lubrication theory for $\mu = 0.91$ mPa s is also shown (red solid line). Hence, it is possible to infer that the experiments of Ozsun *et al.* (2013) took place at a room temperature of approximately 20 °C. Furthermore, our numerical simulations were computed taking $\rho = 10^3$ kg m^{-3}, and $B \simeq 1.6$ μJ, where $B = Ed^3/[12(1-\nu^2)]$ is the bending stiffness of the upper wall. As pointed out by Christov *et al.* (2018), there is uncertainty in the measurements of the bending stiffness B, although the curve q–Δp is less sensitive to changes in B than to changes in the liquid viscosity μ.

Additionally, we have also considered the nonlinear strain (3.9) in some simulations where q and Δp are relatively high (blue crosses). We observe that there is only a small deviation between the linear and nonlinear results, as will be confirmed in § 5, which indicates that the strain is small enough that the linear strain–displacement relationship (3.8) holds.

https://doi.org/10.1017/jfm.2019.994 Published online by Cambridge University Press

$y,\ x,\ z$	$v_y,\ v_x,\ v_z$ (4.6*a*)	Equation (4.6*d*)	Equation (4.6*e*)	Equation (4.6*f*)
$h_0 \ll w \ll \ell,\ d \ll w$	$\frac{h_0}{\ell}V_\ell \ll \frac{w}{\ell}V_\ell \ll V_\ell$	$V_\ell \sim \frac{h_0^2 p_c}{12\mu\ell}$	$u_c \sim \frac{w^4 p_c}{B}$	$t_c \sim \frac{\mu w^4 \ell^2}{B h_0^3}$
$\epsilon \ll \delta \ll 1,\ \alpha \ll 1$	$\frac{O(u_y)}{h_0}$	$\frac{O(\rho \boldsymbol{v}\cdot\boldsymbol{\nabla}\boldsymbol{v})}{O(\mu\nabla^2\boldsymbol{v})}$	$\frac{O(\rho\partial_t \boldsymbol{v})}{O(\mu\nabla^2\boldsymbol{v})}$	$\frac{O(\rho_s d\,\partial_t^2 u_y)}{O(B\nabla^4_{xz}u_y)}$
$\epsilon = \frac{h_0}{\ell},\ \delta = \frac{h_0}{w},\ \alpha = \frac{d}{w}$	$\tilde{\beta} = \frac{w^4 p_c}{240 h_0 B}$	$\frac{\epsilon Re}{12} = \frac{\rho h_0^4 p_c}{144\mu^2\ell^2}$	$\frac{\epsilon Re}{4\tilde{\beta}} = \frac{5\rho h_0^5 B}{\mu^2\ell^2 w^4}$	$\gamma = \frac{\rho_s d h_0^6 B}{\mu^2\ell^4 w^4}$

TABLE 1. Characteristic scales used in the derivation of the unsteady lubrication model of § 4.3 (upper row), and the dimensionless parameters that govern the elasto-hydrodynamic problem, deduced in § 4.2 (bottom row).

A typical 3-D simulation is presented in figure 2(*b*), which shows the pressure field p in the fluid domain and the vertical solid displacement field u_y in the solid domain, under the same conditions as the S4 experiment of Ozsun *et al.* (2013) for an imposed inlet pressure $\Delta p = 6$ kPa. These results correspond to the triangle at the largest value of q in figure 2(*a*).

4. Lubrication theory for shallow compliant channels

This section is devoted to the derivation of an unsteady lubrication theory for a slender, shallow and deformable microchannel with rectangular cross-section, using as a starting point the complete set of (3.1)–(3.12) presented in § 3.

4.1. *Kirchhoff–Love theory for the upper wall deformation*

In developing the lubrication model, the Navier equation (3.7) will be substituted by an appropriate simplified description, based on plate theory, that takes advantage of the upper wall geometry. In particular, if the maximum displacement of the upper wall is small compared to its thickness d, which is constant and smaller than the channel's width w, the dynamics of the plate under pure bending can be described with the Kirchhoff–Love equation (Love 1888; Howell, Kozyreff & Ockendon 2009) with clamped boundary conditions at $x = \pm w/2$. Therefore, the vertical displacement is now independent of y, i.e. $u_y = u_y(x, z, t)$, and satisfies

$$\rho_s d\partial_t^2 u_y + B\nabla^4_{xz} u_y = p \quad \text{at } y = h(x, z, t), \tag{4.1a}$$

$$u_y = 0, \quad \text{and} \quad \partial_z u_y = 0 \quad \text{at } z = 0, \text{ and } z = \ell, \tag{4.1b}$$

$$u_y = 0, \quad \text{and} \quad \partial_x u_y = 0 \quad \text{at } x = \pm w/2, \tag{4.1c}$$

where ∇^4_{xz} is the biharmonic operator in the (x, z) plane, and the bending stiffness $B = Ed^3/[12(1-\nu^2)]$ of the upper wall is assumed constant.

4.2. *Characteristic scales of the unsteady flow*

Here we obtain the characteristic scales and the dimensionless parameters governing the unsteady flow in the coupled elasto-hydrodynamic problem, identifying the conditions under which the set of (3.1)–(3.6) and (4.1*a*)–(4.1*c*) can be approximated by either an unsteady or a quasi-steady lubrication model. First, we set the dominant

https://doi.org/10.1017/jfm.2019.994 Published online by Cambridge University Press

	h_0 (mm)	w (mm)	ℓ (mm)	d (mm)	B (μJ)	ν	ρ_s (kg m^{-3})	Δp (kPa)	$\tilde{\beta}$
S4	0.244	1.7	15.5	0.2	≈1.6	0.499	970	4.487	0.4

	ρ (kg m^{-3})	μ (Pa s)	q_0 (ml min^{-1})	$\frac{\epsilon Re}{12}$	$\frac{\epsilon Re}{4\tilde{\beta}}$	$\tilde{\gamma}$
Case I	970	0.485	7.38×10^{-2}	1.9×10^{-6}	1.42×10^{-5}	2.1×10^{-6}
Case II	10^3	10^{-3}	35.76	0.46	3.45	0.49

TABLE 2. Physical parameters corresponding to the S4 experiment of Ozsun *et al.* (2013) for two different working liquids, namely water (II), which is the least favourable configuration, and a silicon oil of 500 cSt (I), for which the assumptions of § 4.5 are satisfied. The values of q_0 and Δp ensure that $\tilde{\beta} = 0.4$, both in the pressure-controlled case and in the flow-rate-controlled situation.

balances that govern the problem by taking advantage of the geometry of the microchannel and its top wall, which both are slender and narrow, i.e. $h_0 \ll w \ll \ell$, and $d \ll w$. These scales imply the hierarchy $\epsilon \ll \delta \ll 1$, and $\alpha \ll 1$, where $\epsilon = h_0/\ell$, $\delta = h_0/w$ and $\alpha = d/w$ measure the slenderness and the shallowness of the channel, and the narrow geometry of the plate, respectively. The three dominant balances come from, respectively, the standard lubrication force balance in the z-direction $\partial_z p \sim \mu \partial_y^2 v_z$, the narrow-geometry plate balance in (4.1*a*) $B\partial_x^4 u_y \sim p$ and the flux balance $\partial_t u_y \sim v_y \sim \epsilon V_\ell$. The latter can be also deduced from the Reynolds equation

$$\int_{-w/2}^{w/2} (\partial_t u_y)\, \mathrm{d}x + \partial_z q = 0, \tag{4.2}$$

where we have used the kinematic condition at the liquid–solid interface, $\boldsymbol{v} \cdot \boldsymbol{n} = \boldsymbol{n} \cdot \partial_t \boldsymbol{u}$, which yields $\partial_t u_y + v_x \partial_x u_y + v_z \partial_z u_y = v_y$, assuming that the displacement is only in the y-direction, $\boldsymbol{u} = (0, u_y, 0)$.

Using the balances above, the following relations are obtained:

$$V_\ell \sim \frac{h_0^2 p_c}{12\mu\ell}, \quad u_c \sim \frac{w^4 p_c}{B} \quad \text{and} \quad t_c \sim \frac{u_c \ell}{h_0 V_\ell} \sim \frac{12\mu\ell^2 w^4}{B h_0^3}, \tag{4.3a–c}$$

where p_c, V_ℓ, u_c and t_c are the characteristic pressure, axial velocity, top wall displacement and time scale, respectively. In particular, the characteristic pressure is $p_c \sim \Delta p$ in a pressure-controlled configuration or $p_c \sim 12\mu\ell q_0/(w h_0^3)$ in a flow-rate-controlled situation, where the factor 12 is the classical lubrication factor. Note that t_c does not depend on Δp or q_0, but only on the geometry and on the fluid and solid properties.

The convective acceleration of the fluid can be neglected compared with the viscous force in (3.1) when $O(\rho \boldsymbol{v} \cdot \nabla \boldsymbol{v})/O(\mu \nabla^2 \boldsymbol{v}) \sim \epsilon Re = (h_0/\ell)\rho h_0^3 p_c/(12\mu^2\ell) \ll 1$, where Re is the Reynolds number based on the characteristic pressure p_c and on the undeformed height h_0. The local acceleration of the fluid in (3.1) is negligible when the viscous diffusion time, $\rho h_0^2/\mu$, is much smaller than the characteristic hydro-elastic time t_c, i.e. when $O(\rho \partial_t \boldsymbol{v})/O(\mu \nabla^2 \boldsymbol{v}) \sim 12\epsilon Re/\beta = \rho h_0^5 B/(\mu^2 \ell^2 w^4) \ll 1$, which is the so-called Womersley number, and where $\beta = u_c/h_0 = w^4 p_c/(h_0 B)$ is the compliance

https://doi.org/10.1017/jfm.2019.994 Published online by Cambridge University Press

parameter. Furthermore, the inertia of the top wall can be neglected in (4.1*a*) when the characteristic time for which the inertia of the solid affects its displacement, t_s, is much smaller than the characteristic start-up time involving the deflection of the boundary, t_c, i.e. when $O(\rho_s d\partial_t^2 u_y)/O(B\nabla_{xz}^4 u_y) \sim \gamma = (t_s/t_c)^2 = \rho_s d h_0^6 B/(\mu^2 \ell^4 w^4) \ll 1$. Note that, like t_c, the dimensionless numbers $\epsilon Re/\beta$ and γ do not depend on Δp or q_0, but only on the geometry of the channel and on the solid and fluid properties.

As shown below, a more precise estimate provides $t_c \sim \mu \ell^2 w^4/(60 B h_0^3)$, which leads to a modified parameter $\tilde{\gamma} = 60^2\gamma$. It also proves convenient to define a modified compliance parameter $\tilde{\beta} = \beta/240$, which is ten times smaller than the one used by Christov *et al.* (2018). As will be shown in § 4.3, a more accurate estimate of the local and convective inertia is $\epsilon Re/(4\tilde{\beta})$, and $\epsilon Re/12$, respectively. Taking typical values from the experimental data of Ozsun *et al.* (2013), who used water as the working liquid, $\tilde{\beta} \sim 1$, $\epsilon Re \sim 1$ and $\tilde{\gamma} \sim 1$. However, it is important to note that $\epsilon Re/(4\tilde{\beta}) \propto \mu^{-2}$ and $\tilde{\gamma} \propto \mu^{-2}$, so that both dimensionless parameters rapidly become small as the liquid viscosity increases. Therefore, the flow is governed by six dimensionless parameters, namely ϵ, δ, α, $\tilde{\beta}$, ϵRe and $\tilde{\gamma}$:

$$\epsilon = \frac{h_0}{\ell}, \quad \delta = \frac{h_0}{w}, \quad \alpha = \frac{d}{w}, \quad \tilde{\beta} = \frac{w^4 p_c}{240 h_0 B}, \quad \epsilon Re = \frac{\rho h_0^4 p_c}{12\mu^2 \ell^2}, \quad \tilde{\gamma} = \frac{60^2 \rho_s d h_0^6 B}{\mu^2 \ell^2 w^4}, \tag{4.4a–f}$$

where the only non-geometrical parameters are $\tilde{\beta}$, Re and $\tilde{\gamma}$. Table 1 summarises the analysis on the characteristic scales presented herein, and the dimensionless parameters governing the problem.

Characteristic times equivalent to those deduced above have been obtained previously. For instance, in the same configuration as ours, Dendukuri *et al.* (2007) deduced similar scalings under the assumption that the spanwise average of the upper wall's vertical displacement is linearly proportional to the fluid pressure. However, as shown below, such an assumption leads to a free parameter and cannot describe most channel geometries. Furthermore, following the latter procedure, Tabeling (2005) deduced the characteristic time scale of a deformable cylindrical chamber pumping fluid into a much smaller microfluidic channel, which gives rise to the bottleneck effect, where, due to the deformation of the reservoir, the start-up time increases from minutes to hours. In contrast, Elbaz & Gat (2014, 2016) obtained the characteristic start-up time without adjustable parameters, following a procedure similar to that developed in the previous paragraph, but in the case of a cylindrical elastic tube conveying a viscous fluid, including the presence of an inner coaxial rigid cylinder.

4.3. *Non-dimensional formulation*

We define the following dimensionless variables:

$$X = \frac{x}{w}, \quad Y = \frac{y}{h_0}, \quad Z = \frac{z}{\ell}, \quad T = \frac{60 h_0^3 B}{\mu w^4 \ell^2} t, \quad H = \frac{h}{h_0}, \quad U_Y = \frac{B}{w^4 p_c} u_y, \tag{4.5a–f}$$

$$V_X = \frac{\delta}{\epsilon} \frac{12\mu\ell}{h_0^2 p_c} v_x, \quad V_Y = \frac{1}{\epsilon} \frac{12\mu\ell}{h_0^2 p_c} v_y, \quad V_Z = \frac{12\mu\ell}{h_0^2 p_c} v_z, \quad P = \frac{p}{p_c}, \quad Q = \frac{12\mu\ell}{w h_0^3 p_c} q, \tag{4.5g–k}$$

where $p_c = \Delta p$, in a pressure-controlled situation, and $p_c = 12\mu\ell q_0/(w h_0^3)$ in a flow-rate-controlled configuration. Introducing these variables into (3.1), (4.1*a*) and (4.2) provides the following dimensionless equations:

https://doi.org/10.1017/jfm.2019.994 Published online by Cambridge University Press

$$\boldsymbol{\nabla}\cdot\boldsymbol{V}=0, \tag{4.6a}$$

$$12\left[\frac{\epsilon^2}{\delta^2}\left(\frac{\epsilon Re}{4\tilde{\beta}}\partial_T V_X+\frac{\epsilon Re}{12}\boldsymbol{V}\cdot\boldsymbol{\nabla}V_X\right)+\partial_X P\right]=\epsilon^2\partial_X^2 V_X+\frac{\epsilon^2}{\delta^2}\partial_Y^2 V_X+\frac{\epsilon^4}{\delta^2}\partial_Z^2 V_X, \tag{4.6b}$$

$$12\left[\epsilon^2\left(\frac{\epsilon Re}{4\tilde{\beta}}\partial_T V_Y+\frac{\epsilon Re}{12}\boldsymbol{V}\cdot\boldsymbol{\nabla}V_Y\right)+\partial_Y P\right]=\epsilon^2\delta^2\partial_X^2 V_Y+\epsilon^2\partial_Y^2 V_Y+\epsilon^4\partial_Z^2 V_Y, \tag{4.6c}$$

$$12\left(\frac{\epsilon Re}{4\tilde{\beta}}\partial_T V_Z+\frac{\epsilon Re}{12}\boldsymbol{V}\cdot\boldsymbol{\nabla}V_Z+\partial_Z P\right)=\delta^2\partial_X^2 V_Z+\partial_Y^2 V_Z+\epsilon^2\partial_Z^2 V_Z, \tag{4.6d}$$

$$\tilde{\gamma}\,\partial_T^2 U_Y+\partial_X^4 U_Y+\frac{\epsilon^2}{\delta^2}2\partial_X^2\partial_Z^2 U_Y+\frac{\epsilon^4}{\delta^4}\partial_Z^4 U_Y=P, \tag{4.6e}$$

$$720\int_{-1/2}^{1/2}(\partial_T U_Y)\mathrm{d}X+\partial_Z Q=0, \tag{4.6f}$$

$$Q(Z,T)=\int_{-1/2}^{1/2}\int_0^{1+\beta U_Y(X,Z,T)} V_Z\,\mathrm{d}Y\,\mathrm{d}X, \tag{4.6g}$$

together with the dimensionless version of the boundary conditions, which are omitted here for simplicity. Here $\boldsymbol{V}=(V_X, V_Y, V_Z)$ is the dimensionless velocity vector.

The elasto-hydrodynamic time scale t_c is the characteristic time for the channel to transition from the undeformed state to the deformed steady state. For a given channel geometry and working fluid, as the rigidity of the wall increases ($B\to\infty$ and hence $\beta\to 0$) the time scale t_c decreases, reflecting the fact that less time is required to inflate the channel to the less deformed final steady state ($u_c\to 0$). For a perfectly rigid channel ($\beta=0$), the transition occurs instantaneously (in the absence of fluid inertia). Since t is non-dimensionalised using t_c (4.5), in the limit $\beta\to 0$ the non-dimensional equations obtained below remain regular and tend towards a limiting solution, which we investigate in appendix A.

4.4. *Leading-order lubrication model*

Assuming $\epsilon\ll\delta\ll 1$, $\epsilon Re\ll 1$ and $\tilde{\beta}\gg\epsilon Re$, the X- and Y-momentum equations (4.6*b*) and (4.6*c*) yield $\partial_X P=\partial_Y P=0$, so that the pressure field is only a function of the axial coordinate Z and time T, i.e. $P=P(Z,T)$. Therefore, at leading order, the set of (4.6*a*)–(4.6*g*) yields the following system of nonlinear differential equations:

$$12\partial_Z P=\partial_Y^2 V_Z, \tag{4.7a}$$

$$\tilde{\gamma}\,\partial_T^2 U_Y+\partial_X^4 U_Y=P, \tag{4.7b}$$

$$720\int_{-1/2}^{1/2}(\partial_T U_Y)\,\mathrm{d}X+\partial_Z Q=0, \tag{4.7c}$$

$$Q(Z,T)=\int_{-1/2}^{1/2}\int_0^{1+\beta U_Y(X,Z,T)} V_Z\,\mathrm{d}Y\,\mathrm{d}X. \tag{4.7d}$$

Note that the leading-order lubrication equations (4.7*a*)–(4.7*d*) cannot fulfil all of the boundary conditions of the full set of equations. In particular, the no-slip boundary condition (3.2) is not satisfied at the sidewalls $X=\pm 1/2$, and from the kinematic condition (3.6), only the no-slip condition $V_Z=0$ remains to be imposed at $Y=H(X,Z,T)$. In addition, the clamped conditions (4.1*b*) cannot be imposed on the upper wall. Therefore, the sidewall boundary conditions for V_Z, and

https://doi.org/10.1017/jfm.2019.994 Published online by Cambridge University Press

the inlet and outlet boundary conditions for U_Y, lead to corrections of the order of $O(\delta) \ll 1$ and $O(\epsilon/\delta) \ll 1$ respectively, as discussed by Christov *et al.* (2018). Hence, equations (4.7*a*)–(4.7*d*) must be complemented with the boundary and initial conditions,

$$V_Z = 0 \quad \text{at } Y = 0, \quad \text{and} \quad Y = H(X, Z, T) = 1 + \beta U_Y(X, Z, T), \tag{4.8a}$$

$$U_Y = 0, \quad \text{and} \quad \partial_X U_Y = 0 \quad \text{at } X = \pm 1/2, \tag{4.8b}$$

$$\left.\begin{array}{ll} Q = 1, & \textit{flow-rate-controlled} \\ P = 1, & \textit{pressure-controlled} \end{array}\right\} \quad \text{at } Z = 0, \tag{4.8c}$$

$$P = 0 \quad \text{at } Z = 1. \tag{4.8d}$$

In the present work, instead of tackling the complex set of (4.7*a*)–(4.8*d*), we will just consider the case of negligible solid inertia, corresponding to the limit $\tilde{\gamma} \to 0$.

4.5. *The limit* $\tilde{\gamma} \to 0$

In the limit $\tilde{\gamma} \to 0$, equations (4.7*a*)–(4.8*d*) provide, at leading order, the quasi-steady description

$$V_Z(X, Y, Z) = -6Y[1 + \beta U_Y(X, Z, T) - Y]\partial_Z P, \tag{4.9a}$$

$$U_Y(X, Z, T) = \frac{P(Z, T)}{24}\left(X^2 - \frac{1}{4}\right)^2, \tag{4.9b}$$

$$Q(Z, T) = -\partial_Z P \int_{-1/2}^{1/2} [1 + \beta U_Y(X, Z, T)]^3 \, \mathrm{d}X = -F(\tilde{\beta}P)\partial_Z P, \tag{4.9c}$$

where

$$F(x) = 1 + x + \frac{10}{21}x^2 + \frac{250}{3003}x^3 \quad \text{and} \quad \tilde{\beta} = \frac{\beta}{240}. \tag{4.10a,b}$$

The Reynolds equation (4.7*c*) yields, using (4.9*b*) and (4.9*c*), a nonlinear diffusion equation for $P(Z, T)$,

$$\partial_T P = \partial_Z[F(\tilde{\beta}P)\partial_Z P], \tag{4.11}$$

subject to the boundary and initial conditions

$$\left.\begin{array}{ll} P = 1, & \textit{pressure-controlled} \\ -F(\tilde{\beta}P)\partial_Z P = 1, & \textit{flow-rate-controlled} \end{array}\right\} \quad \text{at } Z = 0, \tag{4.12a}$$

$$P = 0 \quad \text{at } Z = 1, \tag{4.12b}$$

$$P = 0 \quad \text{at } T = 0, \text{ and } 0 < Z < 1. \tag{4.12c}$$

Note that if the transient is flow-rate controlled, the dimensionless inlet pressure is a function of time, $P_0(T) = P(Z = 0, T)$ in order to impose a constant inlet flow rate $Q_0 = Q(Z = 0, T) = 1$, whose expression can be obtained from (4.9*c*).

4.6. *Self-similar solutions*

Under pressure-controlled conditions, equation (4.11) admits an exact self-similar solution $P = P(\zeta)$ in terms of a rescaled coordinate $\zeta = z/\sqrt{T}$ at early times $T \ll 1$

https://doi.org/10.1017/jfm.2019.994 Published online by Cambridge University Press

before the diffusion front has reached the end of the channel. The profile $P(\zeta)$ satisfies the ordinary differential equation and boundary conditions

$$2(F(\tilde{\beta}P)P')' + \zeta P' = 0, \quad P(\zeta = 0) = 1 \quad \text{and} \quad P(\zeta \to \infty) \to 0, \tag{4.13a–c}$$

where primes indicate derivatives with respect to ζ. Note from (4.9*c*) that the corresponding flow rate is of the form $Q = \varphi(\zeta)/\sqrt{T}$, and the result $Q_0 = \varphi(0)/\sqrt{T}$ is in agreement with the early-time behaviour of the numerical results shown in figure 4(*a*) below. Figure 3 shows P and φ as a function of ζ for several values of $\tilde{\beta}$ indicated in the legend. As $\tilde{\beta}$ increases (e.g. bending modulus decreases), the displacement of the top wall increases and hence a higher pressure and flow rate are achieved within the channel.

For $\tilde{\beta} \ll 1$, the self-similar equation (4.13) becomes the classical diffusion equation with a constant input $P = 1$, with solution

$$P(\zeta) = \operatorname{erfc}\left(\frac{\zeta}{2}\right), \quad Q(\zeta) = \frac{\mathrm{e}^{-(\zeta/2)^2}}{\sqrt{\pi T}}. \tag{4.14a,b}$$

Equation (4.14*a*,*b*) fits the curves of figure 3 when $\tilde{\beta} \ll 1$ and also the early-time trend $Q_0 = 1/\sqrt{\pi T}$ observed in figure 4(*a*). It also agrees with the early-time behaviour of the small-$\tilde{\beta}$ asymptotic solution (A 4*a*) derived in appendix A.

Moreover, for $\tilde{\beta} \gg 1$, using the approximation $F(\tilde{\beta}P) \approx (250/3003)\tilde{\beta}^3P^3$, the equations (4.11) and (4.13) become (after a rescaling) the well-known equations for a viscous gravity current and their self-similar form, which have been solved by Pattle (1959) and Huppert (1982) among others.

Although a flow-rate-controlled configuration does not admit an early-time self-similar solution for general $\tilde{\beta}$, it does so in the limits $\tilde{\beta} \to 0$ and $\tilde{\beta} \to \infty$. First, when $\tilde{\beta} \to 0$, equation (4.11) again becomes the diffusion equation but with constant input flux $-\partial_Z P = 1$, whose self-similar solution is given by

$$P(\zeta) = \sqrt{T}\int_{\zeta}^{\infty} \operatorname{erfc}\left(\frac{s}{2}\right) \mathrm{d}s, \quad Q(\zeta) = \operatorname{erfc}\left(\frac{\zeta}{2}\right). \tag{4.15a,b}$$

The requirement that $F(\tilde{\beta}P) \approx 1$ yields the condition $T \ll \tilde{\beta}^{-2}$ for validity. This result also agrees with the small-$\tilde{\beta}$ asymptotic solution (A 4*b*) derived in appendix A, and the result $P_0 = 2\sqrt{T/\pi}$ agrees with the early-time behaviour of figure 4(*b*) below. In the opposite limit, $\tilde{\beta} \to \infty$, we again obtain the gravity-current equation but with constant input flux, for which the self-similar solution has $Z \sim \tilde{\beta}^{3/5}T^{4/5}$ and $P \sim \tilde{\beta}^{-3/5}T^{1/5}$ (Huppert 1982), and the conditions for validity $\tilde{\beta}P \gg 1$ and $Z \ll 1$ yield $\tilde{\beta}^{-2} \ll T \ll \tilde{\beta}^{-3/4}$.

5. Results

This section is devoted to presenting the results obtained with the quasi-steady lubrication theory developed in § 4.5, and to comparing these results with those extracted from the 3-D numerical simulations described in § 3. The quasi-steady lubrication equation (4.11) was solved numerically with a standard finite-difference scheme. In particular, we have computed the fluid pressure distribution $P(Z, T)$, the associated flow-rate distribution, $Q(Z, T)$, and the vertical wall displacement,

https://doi.org/10.1017/jfm.2019.994 Published online by Cambridge University Press

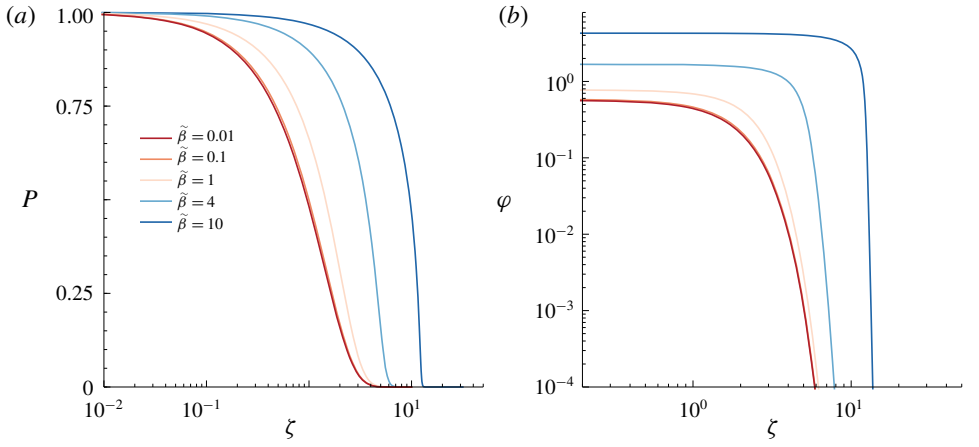


FIGURE 3. Self-similar solution for the pressure-controlled case, showing (*a*) the pressure $P(\zeta)$ and (*b*) the rescaled flow rate $\varphi(\zeta) = Q\sqrt{T}$, for different values of $\tilde{\beta}$ indicated in the legend.

$U_Y(X, Z, T)$, for several values of $\tilde{\beta}$. As shown by Christov *et al.* (2018), higher flow rates are achieved as $\tilde{\beta}$ increases, corresponding to a larger upper wall deformation and a reduced hydraulic resistance. For instance, in a steady pressure-controlled situation, the dimensionless flow rate is higher for a given pressure drop (Christov *et al.* 2018),

$$Q(T \to \infty) \to 1 + \tfrac{1}{2}\tilde{\beta} + \tfrac{10}{63}\tilde{\beta}^2 + \tfrac{125}{6006}\tilde{\beta}^3, \tag{5.1}$$

since the cross-section increases as the top wall deforms. This result can be observed in figure 4(*a*,*b*), which shows the dependence of the inlet flow rate in a pressure-controlled configuration, $Q_0 = Q(Z = 0, T)$ in (*a*), and the inlet overpressure $P_0 = P(Z = 0, T)$ in flow-rate-controlled conditions in (*b*), as a function of time T for several values of $\tilde{\beta}$. The insets show how the solution of Christov *et al.* (2018) (dashed lines) is reached for $T \gtrsim O(1)$, revealing that t_c is indeed the proper time scale. In pressure-controlled configurations Q_0 decreases with time as the initial condition for the fluid pressure diffuses along the channel and $\partial_Z P(Z = 0, T)$ decreases in magnitude. In flow-rate-controlled conditions, P_0 increases with time since the magnitude of $\partial_Z P$ decreases as the fluid spreads, so that $F(\tilde{\beta}P)$ must increase to keep $Q_0 = 1$.

To illustrate the diffusion of $P(Z, T)$ and $Q(Z, T)$, and the displacement $\beta U_Y(X = 0, Z, T)$ along the channel, we show in figure 5 (dashed lines) their time evolution for $\tilde{\beta} = 0.4$, under pressure-controlled conditions (*a*) and flow-rate-controlled conditions (*b*). Here, $U_Y(X = 0, Z, T) = U_m(Z, T) = P(Z, T)/384$ is the maximum displacement of the top wall according to (4.9*b*). The results obtained at the largest time indicated in the legend correspond to the steady solution of Christov *et al.* (2018).

5.1. *Start-up time and comparison with previous models*

The dimensionless start-up time at which the steady-state solution of Christov *et al.* (2018) is reached, denoted by T_d, is defined here by the condition $|\partial_T Q(Z = 1, T_d)| = 10^{-4}$. We have ensured that the value of T_d is robust against alternative choices of the dependent variable. For instance, $\max_Z |\partial_T P(Z, T_d)| = 10^{-4}$ provides very similar values. The start-up time is shown in figure 4(*c*,*d*) as a function of $\tilde{\beta}$

https://doi.org/10.1017/jfm.2019.994 Published online by Cambridge University Press

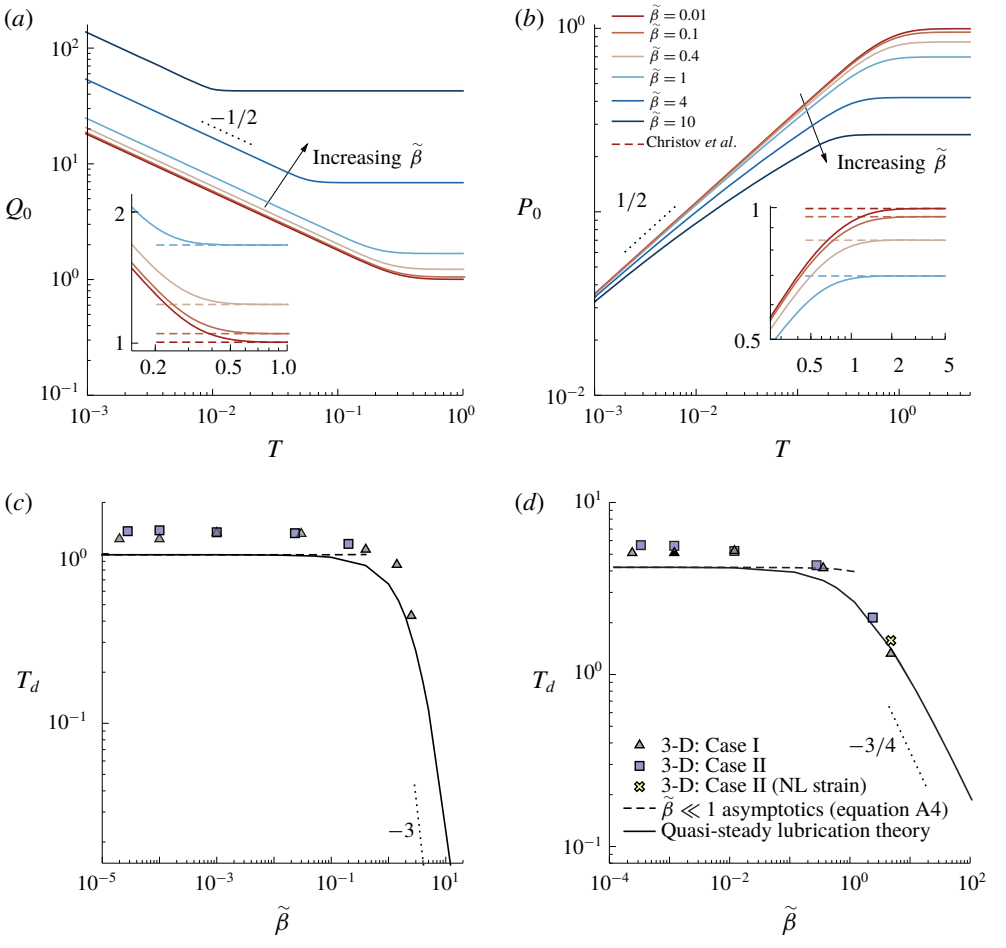


FIGURE 4. (*a*) Inlet flow rate Q_0 for a pressure-controlled channel and (*b*) inlet overpressure P_0 in a flow-rate-controlled configuration, as a function of time T, for several values of $\tilde{\beta}$ as indicated in the legend. The insets show the solution of Christov *et al.* (2018) reached at long time (dashed lines). The start-up time T_d is shown for (*c*) a pressure-controlled configuration and for (*d*) a flow-rate-controlled configuration. The solid lines correspond to the quasi-steady lubrication theory given by equations (4.11)–(4.12*c*). The symbols correspond to the 3-D numerical simulations for two combinations of the dimensionless parameters ϵRe and $\tilde{\gamma}$ reported in table 2, and the dashed lines correspond to the asymptotic solution for $\tilde{\beta} \ll 1$ obtained in appendix A.

in a pressure-controlled and in a flow-rate-controlled configuration, respectively, computed with the quasi-steady lubrication model (4.11), with the 3-D numerical simulations of § 3, and with the small-deformation ($\tilde{\beta} \ll 1$) asymptotic solutions (A 4) from appendix A. Figure 4(*c*,*d*) reveals that the dimensionless start-up time decreases as the compliance increases. For instance, the value of T_d decreases by a factor of 2 when $\tilde{\beta}$ is increased from 0 to 1.6 (pressure controlled) or 2 (flow-rate controlled). In the limit $\tilde{\beta} \to 0$, the values of T_d reach the corresponding rigid-channel asymptotes, $T_d \simeq 0.98$ and $T_d \simeq 4.2$, when $\tilde{\beta} \lesssim 0.02$ and $\tilde{\beta} \lesssim 0.01$, respectively.

https://doi.org/10.1017/jfm.2019.994 Published online by Cambridge University Press

Consequently, the asymptotic solutions developed in appendix A for $\tilde{\beta} \ll 1$ are valid for $\tilde{\beta} \lesssim 0.01$. In the opposite limit, $\tilde{\beta} \gg 1$, we can obtain the scalings $T_d \propto \tilde{\beta}^{-3}$ for a pressure-controlled configuration, and $T_d \propto \tilde{\beta}^{-3/4}$ for a flow-rate-controlled situation, from the gravity-current solutions deduced in § 4.6, or by setting $u_c \sim h_0$ in the scaling arguments of § 4.2.

The results of the 3-D numerical simulations shown in figure 4(*c*,*d*) were computed for the geometry of the S4 experiment of Ozsun *et al.* (2013), different values of $\tilde{\beta}$ and two different combinations of ϵRe and $\tilde{\gamma}$, corresponding to two different working liquids (see table 2). Case I corresponds to a silicon oil of viscosity 500 cSt as working liquid, where $\epsilon Re/12 = 1.9 \times 10^{-6}$ and $\tilde{\gamma} = 2.1 \times 10^{-6}$ (triangles), and case II corresponds to water, which is the least favourable case for this S4 geometry since $\epsilon Re/12 = 0.46$ and $\tilde{\gamma} = 0.49$ (squares), and thus the inertia of the liquid and of the solid may have influence on the flow. However, we have found fair agreement between the quasi-steady lubrication model with negligible solid and liquid inertia and the 3-D numerical simulations in both cases. In particular, the agreement improves for increasing values of $\tilde{\beta}$, indicating that the relative importance of the solid and liquid inertia becomes smaller for larger wall displacements. In particular, the local liquid inertia becomes negligible as $\tilde{\beta} \to \infty$, since $\epsilon Re/(4\tilde{\beta}) \to 0$. Moreover, $\tilde{\gamma}$ can be expressed in terms of $\tilde{\gamma} \propto \rho_s d h_0^2 p_c \epsilon^3/(12\mu^2 \ell \tilde{\beta})$, so that the solid inertia becomes negligible as $\tilde{\beta}$ increases for a fixed geometry and liquid.

We have also considered the lubrication model derived by Dendukuri *et al.* (2007), and later used by Panda *et al.* (2009), in which the spanwise average of the upper wall's displacement is assumed to be linearly proportional to the fluid pressure, and thereby the pressure and the displacement fields are only functions of time and the longitudinal coordinate. This type of approximation is usually known as the Winkler foundation (Kerr 1964). To obtain the dimensionless version of their model we take the characteristic displacement as $u_c^D = w p_c/E$, and the characteristic time as $t_c^D = \mu \ell^2 w/(12 E h_0^3)$. Hence, the new dimensionless variables are $t = \mu \ell^2 w/(12 E h_0^3)\mathcal{T}$ and $u_y = (w p_c/E)\mathcal{U}_Y$, and the nonlinear diffusion equation for $P(Z, \mathcal{T})$ reads

$$\partial_{\mathcal{T}} P = \partial_Z [\partial_Z P (1 + \mathscr{D} P)^3] \tag{5.2}$$

subjected to the same boundary and initial conditions as (4.11), and where $\mathscr{D} = w p_c/(h_0 E)$ is the associated compliance parameter. Note that, when $\tilde{\beta} \ll 1$ and $\mathscr{D} \ll 1$, equations (4.11) and (5.2) coincide at leading order: $\partial_{\mathcal{T}} P = \partial_Z^2 P + O(\tilde{\beta})$, or $\partial_{\mathcal{T}} P = \partial_Z^2 P + O(\mathscr{D})$. However, since the scalings for the pressure and the displacement field are different from our lubrication model, the ratios between the different characteristic scales and the two compliance parameters depend on ν and on the ratio w/d, namely $t_c/t_c^D = 12/5(1-\nu^2)(w/d)^3$, $u_c/u_c^D = 12(1-\nu^2)(w/d)^3$, and $\tilde{\beta}/\mathscr{D} = (1-\nu^2)/20(d/w)^3$. Taking the S4 experiment of Ozsun *et al.* (2013) with water as the working liquid (see table 2), and considering $\tilde{\beta} = 0.4$ as a typical configuration, then $\mathscr{D} = 0.017$, and the dimensional steady-state times predicted by each model are $t_d = 1.22$ ms (present work) and $t_d = 1.42$ µs (Dendukuri *et al.* 2007; Panda *et al.* 2009), whose ratio is of the same order as t_c/t_c^D for the parameter values in table 2. Hence, there is a strong quantitative disagreement between the unsteady lubrication model of Dendukuri *et al.* (2007), with both our lubrication theory, and the 3-D numerical simulations. We thus conclude that the model of Dendukuri *et al.* (2007) fails to predict the transient flow, especially in microchannels where the thickness of the top wall is smaller than, or of the same order as, the channel width.

https://doi.org/10.1017/jfm.2019.994 Published online by Cambridge University Press

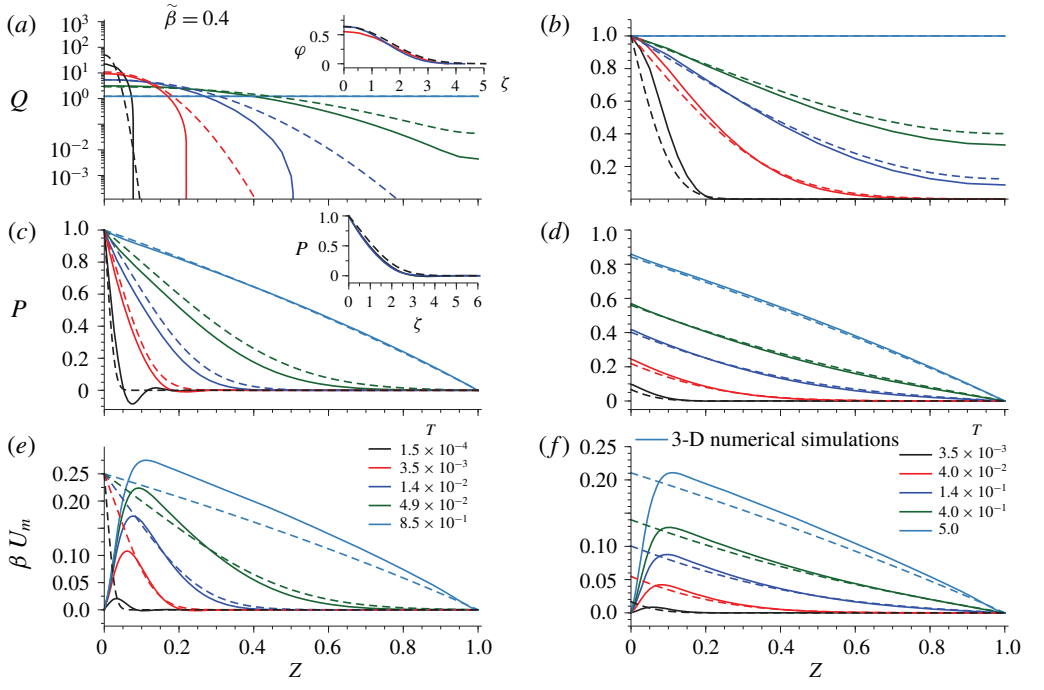


FIGURE 5. Flow rate $Q(Z, T)$, pressure field $P(Z, T)$ and maximum displacement βU_m, as functions of Z for $\tilde{\beta} = 0.4$ at different times indicated in the legend. The system is pressure driven in (*a*,*c*,*e*), and flow-rate controlled in (*b*,*d*,*f*). The dashed lines show the lubrication solution, and the solid lines the 3-D numerical simulations. Here, $\epsilon Re/12 \simeq 1.9 \times 10^{-6}$, $\epsilon Re/(4\tilde{\beta}) \simeq 1.42 \times 10^{-5}$ and $\tilde{\gamma} \simeq 2.1 \times 10^{-6}$, fulfilling the lubrication hypotheses (case I in table 2). The insets show the self-similar solution given by (4.13), together with the rescaled numerical solution for two different times near start-up.

This situation resembles the shortcomings found in previous steady lubrication models (Gervais *et al.* 2006; Hardy *et al.* 2009; Cheung *et al.* 2012; Raj & Sen 2016; Raj *et al.* 2017), in that the fitting parameters that appear in these models have been used even for microchannels with thin upper walls, as pointed out by Christov *et al.* (2018). Indeed, just like these fitting parameters, $\mathscr{D}$ naively absorbs the geometric and material constants.

5.2. *Transient comparison between the quasi-steady lubrication theory and the 3-D numerical simulations*

To perform a more detailed comparison between the results of the quasi-steady lubrication model (4.11)–(4.12*c*) and the 3-D simulations, we have chosen the S4 experiment of Ozsun *et al.* (2013), whose fixed geometrical and physical parameters are reported in table 2. We have also taken $\tilde{\beta} = 0.4$ as a typical value of the compliance parameter, and thus Δp and q_0 (or V_ℓ) are chosen to ensure this value in a pressure-controlled and in a flow-rate-controlled situation, respectively. In the experimental results reported by Ozsun *et al.* (2013) water was used as working liquid, which corresponds to case II of table 2 and is an unfavourable case that does not fulfil the lubrication assumptions of § 4.5. Note that the latter case corresponds to one

https://doi.org/10.1017/jfm.2019.994 Published online by Cambridge University Press

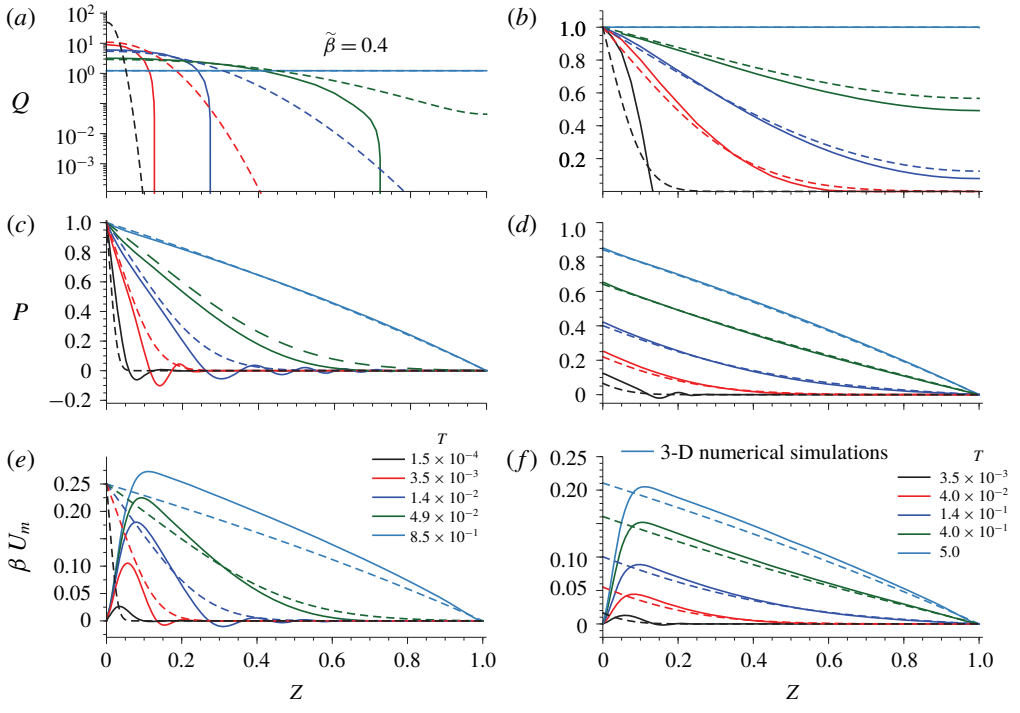


FIGURE 6. Same as figure 5, but for $\epsilon Re/12 \simeq 0.46$, $\epsilon Re/(4\tilde{\beta}) \simeq 3.45$ and $\tilde{\gamma} \simeq 0.49$, corresponding to the conditions of the S4 experiment of Ozsun *et al.* (2013) and case II in table 2.

of the results of the steady 3-D simulations shown in figure 2(*a*), which is in excellent agreement with the experiments. We have also considered a more favourable case, namely case I of table 2, so that the hypotheses behind (4.11)–(4.12*c*) are satisfied.

Figures 5 and 6 show the flow rate Q (*a*,*b*), the pressure distribution P (*c*,*d*) and the displacement of the wall βU_m (*e*,*f*) as functions of Z at different times indicated in the legend, obtained from the lubrication theory (dashed lines) and from the 3-D simulations (solid lines). In both figures, the configuration is pressure controlled in the left column, and flow-rate controlled in the right column. In the 3-D simulations, the pressure drop is evaluated along the line $X = 0$, $Y = 1/2$, while the solid deformation field is evaluated at the fluid–solid interface and $X = 0$. The control parameters correspond to case I in figure 5 and to case II in figure 6.

In case I, the agreement in the time evolution of Q, P and U_m is fairly good both in the pressure-driven and in the flow-rate-controlled configurations, as evidenced by figure 5. In particular, the self-similar solution $P(\zeta)$, $\varphi(\zeta)$ given by (4.13) correctly describes the rescaled numerical solution, as shown by the insets in figure 5(*a*,*c*). In this case, since $\epsilon Re/12$, $\epsilon Re/(4\tilde{\beta})$, $\tilde{\gamma} \ll 1$, the largest source of error is probably the fact that the lubrication approximation does not satisfy the no-slip condition for $\boldsymbol{v}$ at the lateral walls, nor does it satisfy the clamped condition for $\boldsymbol{u}$ at the inlet, which gives rise to an elastic boundary layer where the largest disagreement takes place, especially for U_m. However, as pointed out by Christov *et al.* (2018), its influence is confined to a region of length $O(\epsilon/\delta) \ll 1$. An asymptotic analysis of this boundary layer could be performed following a similar strategy as Elbaz &

https://doi.org/10.1017/jfm.2019.994 Published online by Cambridge University Press

Gat (2016). Additionally, the lubrication approximation is not able to capture the early-time oscillations experienced by P and U_m close to the inlet. These travelling waves are always present even when ϵRe and $\tilde{\gamma}$ are exactly zero. Hence, a possible explanation might be that the derivatives $\partial_z^4 u_y$ and $\partial_z^2 \partial_x^2 u_y$ are significant at early time since their characteristic length scale is $Z \sim 0.05$–0.1, which is of the same order as δ for the geometry considered in cases I and II. Therefore, the Z-scale is initially small as the fluid spreads within the channel causing the oscillations, which eventually disappear as the fluid propagates and the Z-scale increases. An analogous phenomenon has been observed by Lister, Peng & Neufeld (2013), where they found travelling-wave solutions for the peeling of an axisymmetric elastic sheet.

In case II, although the values of $\epsilon Re/12$, $\epsilon Re/(4\tilde{\beta})$ and $\tilde{\gamma}$ are not strictly small, and the lubrication hypotheses are not satisfied, the agreement between the 3-D simulations and the quasi-steady approximation is better than might be expected, as shown by the results in figure 6. However, in this case, the amplitude and the dissipation time of the early-time oscillations of P and U_m are larger, and they also propagate downstream to larger values of Z. This behaviour breaks the self-similarity of P and Q in the pressure-controlled configuration.

Finally, to provide a better illustration of the agreement between the quasi-steady lubrication model and the 3-D numerical simulations, we have also computed the time-dependent evolution of the longitudinal velocity V_Z and the vertical displacement βU_Y at a longitudinal station close to the inlet, $Z = 0.25$, under flow-rate-controlled conditions, and for the values of case II in table 2, i.e. the least favourable configuration, but for $\tilde{\beta} = 4.8$, in order to also test the validity of the linear-strain approximation (3.8). These conditions correspond to an inlet flow rate of $q_0 = 429$ ml min^{-1}, whereas the maximum flow rate reported in the experiments of Ozsun *et al.* (2013) is $q_0 = 50$ ml min^{-1} (see figure 2). Figure 7 displays six different time snapshots, the last one corresponding to the steady state, showing V_Z and βU_Y obtained from the quasi-steady lubrication model (4.11)–(4.12*c*) in the column (*a–f*), from the 3-D numerical simulations using the linear strain (3.8) in the column (*g–l*) and using the nonlinear strain (3.9) in the column (*m–r*). Taking into account that the hypotheses behind the lubrication model (4.11)–(4.12*c*) are not strictly satisfied, the overall agreement between the quasi-steady model and the 3-D simulations during the whole start-up transient is quite good. However, again, there are marked differences between both approaches, e.g. in the no-slip condition at the lateral bounding walls, which the lubrication model cannot fulfil, or the constant thickness and the unidirectional displacement of the top wall considered by the bending-dominated Kirchhoff–Love theory, which do not apply in this configuration where the top wall thickness is comparable to the channel width. Furthermore, the quasi-steady lubrication model slightly underestimates the axial velocity of the fluid and the vertical displacement.

Comparing the 3-D numerical results (*g–l*) and (*m–r*) for linear (3.8) and nonlinear (3.9) strains, respectively, we find that in this case, even though $\tilde{\beta}$ is relatively large and the deflection is comparable to the thickness of the elastic wall, the nonlinear stretching of the wall has a negligible effect on its elastic response, and the linear-strain model is adequate.

6. Conclusions

In this paper we have studied the start-up flow in a shallow rectangular microchannel with a deformable top wall, considering both pressure-controlled and flow-rate-controlled conditions. To that end, we have developed an unsteady lubrication

https://doi.org/10.1017/jfm.2019.994 Published online by Cambridge University Press

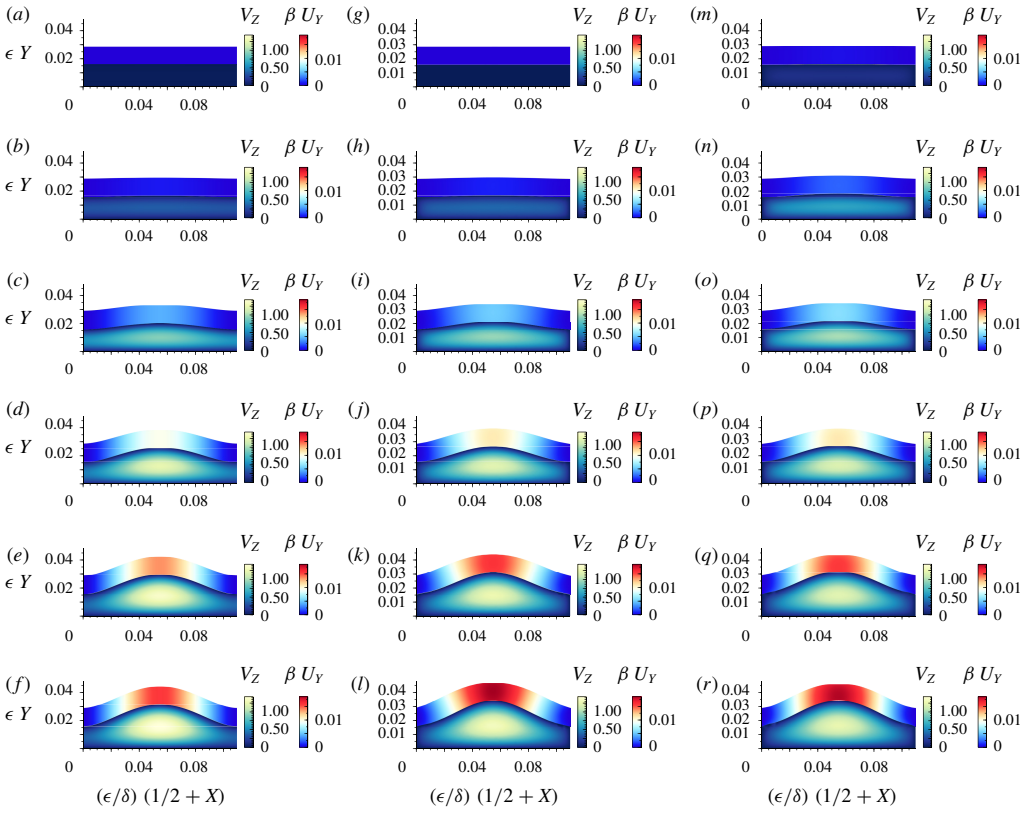


FIGURE 7. Colour plot of longitudinal velocity V_Z and vertical displacement βU_Y in the (X, Y) plane at a station $Z = 0.25$ and times $T = 3.5 \times 10^{-3}$, 1.8×10^{-2}, 5.3×10^{-2}, 1.4×10^{-1}, 2.8×10^{-1} and 7.0×10^{-1}, in (*a–f*), extracted from the quasi-steady lubrication model (4.11)–(4.12*c*), in (*g–l*), extracted from 3-D numerical simulations using the linear strain (3.8) and in (*m–r*) using the nonlinear strain (3.9), for $\tilde{\beta} = 4.8$ under flow-rate-controlled conditions. The values of the parameters correspond to those of figure 6(*b*,*d*,*f*) (case II in table 2).

model, where the top wall is modelled with the Kirchhoff–Love plate theory in the bending-dominated limit. To derive this simplified model we have first identified the characteristic scales and the dimensionless parameters governing the hydro-elastic problem showing, in particular, that the characteristic start-up time only depends on the geometry of the channel and on the solid and fluid properties, but not on the characteristic pressure and flow rate. When the solid and liquid inertia are negligible, the lubrication model is quasi-steady and reduces to a nonlinear diffusion equation for the fluid pressure field, whose only dimensionless parameter is the compliance parameter $\tilde{\beta}$ and that, under pressure-controlled conditions, admits a self-similar solution.

To check the validity of the hypotheses behind the lubrication model in the limit of negligible solid and liquid inertia, we have conducted 3-D numerical simulations of the complete Navier and Navier–Stokes equations for the solid and for the fluid, respectively. In particular, as a basis for comparison, we have selected a microchannel whose geometry corresponds to the S4 experiment of Ozsun *et al.* (2013), and two

https://doi.org/10.1017/jfm.2019.994 Published online by Cambridge University Press

working liquids. First, we have considered a silicon oil of 500 cSt dynamic viscosity, which fulfils the hypotheses, and we have found excellent agreement between the pressure, displacement and flow rate predicted by the quasi-steady lubrication model, and those obtained from the 3-D numerical simulations. In the second case we have considered water as working liquid, for which the liquid and solid inertia are not negligible, although its influence is moderate. In this case we have also obtained fair agreement. We have also derived a leading-order asymptotic solution in terms of a regular expansion in the compliance parameter $\tilde{\beta}$, which properly captures the transient dynamics of the microchannel when $\tilde{\beta} \ll 1$.

We have also computed the start-up time for several values of $\tilde{\beta}$, comparing the values predicted by our lubrication model with those obtained from the model of Dendukuri *et al.* (2007) and from the 3-D numerical simulations. In the two flow configurations considered herein, we have obtained good agreement between the simulations and our model, but not with the lubrication approximation of Dendukuri *et al.* (2007). The reason is that these authors assume that the pressure scales as $p_c \sim u_c E/w$, which is only valid if the elastic wall is large enough, but not when the thickness of the wall is smaller than, or of the same order as, the channel width, where the appropriate scaling is $p_c \sim u_c B/w^4$.

There are many extensions of the present work that deserve further effort. First of all, the inertial corrections associated with finite values of ϵRe and $\tilde{\gamma}$ in the lubrication equations (4.7*a*)–(4.8*d*) should be studied. In addition, other unsteady processes like pulsatile flows should be addressed. For intermediate and large wall thicknesses, the bending-dominated Kirchhoff–Love plate theory fails, and thus stretching and shear have to be included in the modelling, which could be addressed along the lines of Shidhore & Christov (2018) for steady flow. Finally, the case of a microchannel embedded in an elastic half-space should also be studied, since it occurs frequently in applications.

Acknowledgements

The authors are grateful to J. Rivero-Rodríguez and B. Scheid for key numerical advice, to I. C. Christov for pointing out a mistake in figure 2 of an earlier version of the manuscript, and to R. Zaera for helpful discussions. A.M.-C. and A.S. thank the Spanish MINECO, Subdirección General de Gestión de Ayudas a la Investigación, for its support through projects DPI2014-59292-C3-1-P and DPI2015-71901-REDT, and the Spanish MCIU-Agencia Estatal de Investigación through project DPI2017-88201-C3-3-R. These research projects have been partly financed through FEDER European funds. A.M.-C. also acknowledges support from the Spanish MECD through the grant FPU16/02562 and to its associated programme Ayudas a la Movilidad 2018 during his stay at the Complex Fluids Group in Princeton. H.A.S. thanks the NSF for support via CMMI-1661672 and through Princeton University's Material Research Science and Engineering Center DMR-1420541.

Declaration of interests

The authors report no conflict of interest.

Appendix A. The small-compliance limit, $\tilde{\beta} \ll 1$

To study the limit $\tilde{\beta} \ll 1$, we expand the pressure field in $\tilde{\beta}$ as

$$P(Z, T; \tilde{\beta}) = P^{(0)}(Z, T) + \tilde{\beta} P^{(1)}(Z, T) + O(\tilde{\beta}^2). \tag{A 1}$$

https://doi.org/10.1017/jfm.2019.994 Published online by Cambridge University Press

At leading order, using $F(\tilde{\beta}P) \approx 1$, the governing equation (4.11) simplifies to the diffusion equation

$$\partial_T P^{(0)} = \partial_Z^2 P^{(0)}, \tag{A 2}$$

with boundary and initial conditions

$$\left.\begin{array}{ll} P^{(0)}(Z=0,T)=1, & \textit{pressure controlled} \\ -\partial_Z P^{(0)}(Z=0,T)=1, & \textit{flow-rate controlled} \end{array}\right\}, \tag{A 3a}$$

$$P^{(0)}(Z=1,T)=0, \quad P^{(0)}(Z,T=0)=0. \tag{A 3b,c}$$

The solutions can be found using, for example, a Fourier expansion, and are given by

$$P^{(0)} = 1 - Z - \sum_{k=1}^{\infty} \frac{2\sin(k\pi Z)\mathrm{e}^{-(k\pi)^2 T}}{k\pi} \quad (\textit{pressure controlled}), \tag{A 4a}$$

$$P^{(0)} = 1 - Z - \sum_{k=1}^{\infty} \frac{8\cos[(2k-1)\pi Z/2]\mathrm{e}^{-(2k-1)^2\pi^2 T/4}}{(2k-1)^2\pi^2} \quad (\textit{flow-rate controlled}). \tag{A 4b}$$

The first-order correction $P^{(1)}$ satisfies the equation

$$\partial_T P^{(1)} - \partial_Z^2 P^{(1)} = \partial_Z(P^{(0)}\partial_Z P^{(0)}), \tag{A 5}$$

with suitable boundary conditions, and can in principle be calculated in the same way, but the leading-order result is sufficient to verify our numerical results for $\tilde{\beta} \ll 1$.

Figure 8 shows a comparison of the inlet flow rate $Q_0(T)$ in a pressure-controlled configuration ($P_0 = 1$) and the inlet overpressure $P_0(T)$ in a flow-rate-controlled configuration ($Q_0 = 1$), between numerical computations of (4.11)–(4.12*c*) and the corresponding leading-order solutions (A 4*a*) and (A 4*b*), respectively. These solutions have been used to obtain the start-up times T_d in the limit $\tilde{\beta} \ll 1$, shown in figure 4(*c*,*d*) (dashed line). Note that the leading-order asymptotic solutions work very well when $\tilde{\beta} \lesssim 0.1$.

Appendix B. Numerical implementation

In this appendix we describe the numerical techniques used to implement the system (3.1)–(3.12). All the equations are written in weak form by means of the corresponding integral scalar product, defined in terms of test functions for the pressure, velocity and displacement fields, i.e. $\tilde{p}$, $\tilde{\boldsymbol{v}}$ and $\tilde{\boldsymbol{u}}$, respectively. By using the Green identities we finally obtain an integral bilinear system of equations for the set of variables and their corresponding test functions. Equation (3.1) reads in weak form

$$\int_{\Omega_f} [\tilde{p}\nabla\cdot\boldsymbol{v} + \rho(\partial_t\boldsymbol{v} + \boldsymbol{v}\cdot\nabla\boldsymbol{v})\cdot\tilde{\boldsymbol{v}} + \boldsymbol{T}:\nabla\tilde{\boldsymbol{v}}]\,\mathrm{d}\Omega_f - \sum_i \int_{\Gamma_f^i} (\boldsymbol{T}\cdot\boldsymbol{n}_f^i)\cdot\tilde{\boldsymbol{v}}\,\mathrm{d}\Gamma_f = 0, \tag{B 1}$$

where Ω_f is the deformable 3-D fluid domain, and Γ_f^i are the boundary surfaces with their corresponding normal vectors $\boldsymbol{n}_f^i$. The flux integral is set to zero at the fluid–solid interface, since the continuity of stress is imposed in the weak-form Navier equation. At the lateral and lower walls the no-slip condition for the velocity field (3.2) is taken

https://doi.org/10.1017/jfm.2019.994 Published online by Cambridge University Press

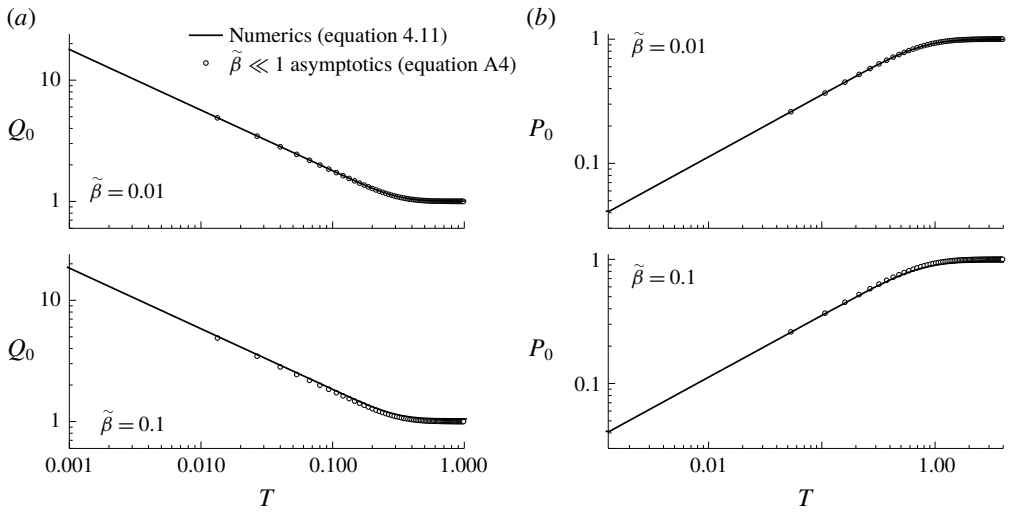


FIGURE 8. Comparison of the inlet flow rate $Q_0(T)$ in a pressure-controlled configuration (*a*) and the inlet overpressure $P_0(T)$ in a flow-rate-controlled configuration (*b*), between numerical computations of (4.11)–(4.12*c*) and corresponding asymptotic solutions at leading order, equations (A 4*a*), and (A 4*b*).

into account by imposing $\tilde{\boldsymbol{v}} = \boldsymbol{0}$ at the corresponding boundaries. At the outlet we impose $\tilde{p} = 0$ as a boundary condition for the pressure field, and also the stress-free boundary condition (3.3). Furthermore, at the inlet, in a pressure-controlled situation we impose a non-homogeneous Dirichlet boundary condition for the pressure and a stress-free boundary condition (3.4). On the other hand, when the microchannel is flow-rate controlled we impose a normal velocity $v_0(x, y)$ corresponding to flow in a rigid channel with the desired flow rate, i.e.

$$(\partial_x^2 + \partial_y^2) v_0 = \text{const.}, \quad v = 0 \quad \text{at} \begin{cases} x = \pm w/2, \\ y = 0, \quad h_0, \end{cases} \qquad \int_{-w/2}^{w/2} \int_0^{h_0} v_0 \, \mathrm{d}y \, \mathrm{d}x = q_0, \tag{B 2}$$

and homogeneous Dirichlet boundary conditions for the tangential velocity (3.5).

The Navier equation (3.7) reads in weak form

$$\int_{\Omega_s} [\rho_s (\partial_t^2 \boldsymbol{u}) \cdot \tilde{\boldsymbol{u}} + \boldsymbol{\sigma} : \nabla \tilde{\boldsymbol{u}}] \, \mathrm{d}\Omega_s - \sum_i \int_{\Gamma_s^i} (\boldsymbol{\sigma} \cdot \boldsymbol{n}_s^i) \cdot \tilde{\boldsymbol{u}} \, \mathrm{d}\Gamma_s^i = 0, \tag{B 3}$$

where Ω_s is the 3-D solid domain, and Γ_s^i are the boundaries with $\boldsymbol{n}_s^i$ the corresponding normal vector. The four clamping conditions (3.10) are imposed as $\tilde{\boldsymbol{u}} = \boldsymbol{0}$ in the flux integral, whereas the continuity of stress (3.11) at the contact interface and the stress-free condition (3.12) at the outer wall are imposed as natural boundary conditions, which read, respectively,

$$\int_{\Gamma_s^{cont}} (\boldsymbol{\sigma} \cdot \boldsymbol{n}) \cdot \tilde{\boldsymbol{u}} \, \mathrm{d}\Gamma_s^{cont} = - \int_{\Gamma_s^{cont}} (\boldsymbol{T} \cdot \boldsymbol{n}) \cdot \tilde{\boldsymbol{u}} \, \mathrm{d}\Gamma_s^{cont} \quad \text{at } y = h(x, z, t), \tag{B 4}$$

$$\int_{\Gamma_s^{ext}} (\boldsymbol{\sigma} \cdot \boldsymbol{n}_{ext}) \cdot \tilde{\boldsymbol{u}} \, \mathrm{d}\Gamma_s^{ext} = 0 \quad \text{at } y = h(x, z, t) + d(x, z, t). \tag{B 5}$$

https://doi.org/10.1017/jfm.2019.994 Published online by Cambridge University Press

Moreover, the continuity of velocity (3.6) is imposed as a weak constraint.

The equations are discretised using Taylor–Hood tetrahedral elements for the pressure and velocity fields, and second-order Lagrange elements for the displacement field, which ensures numerical stability. To account for the deformation of the domain we use the ALE method implemented in COMSOL Multiphysics, where the mesh elements in the solid domain Ω_s move with an imposed displacement given by $\boldsymbol{u}$, whereas in the fluid domain Ω_f they move according to the Laplace equation for the change of variables between the material and the spatial frames (Rivero-Rodríguez & Scheid 2018; Rivero-Rodriguez & Scheid 2019). As for the time stepping, we employ a fourth-order variable-step backward differentiation formula (BDF) method, or an implicit generalised-alpha method when the inertia of the solid becomes relevant (case II). The relative tolerance of the nonlinear method is always set to 10^{-5}.

REFERENCES

ANNA, S. L. 2016 Droplets and bubbles in microfluidic devices. *Annu. Rev. Fluid Mech.* **48**, 285–309.

BICO, J., REYSSAT, É. & ROMAN, B. 2018 Elastocapillarity: when surface tension deforms elastic solids. *Annu. Rev. Fluid Mech.* **50**, 629–659.

BISPLINGHOFF, R. L., ASHLEY, H. & HALFMAN, R. L. 2013 *Aeroelasticity*. Courier Corporation.

BRUUS, H. 2008 *Theoretical Microfluidics*. Oxford University Press.

CANCELLI, C. & PEDLEY, T. J. 1985 A separated-flow model for collapsible-tube oscillations. *J. Fluid Mech.* **157**, 375–404.

CASSOT, F., LAUWERS, F., FOUARD, C., PROHASKA, S. & LAUWERS-CANCES, V. 2006 A novel three-dimensional computer-assisted method for a quantitative study of microvascular networks of the human cerebral cortex. *Microcirculation* **13** (1), 1–18.

CHEUNG, P., TODA-PETERS, K. & SHEN, A. Q. 2012 *In situ* pressure measurement within deformable rectangular polydimethylsiloxane microfluidic devices. *Biomicrofluidics* **6** (2), 026501.

CHRISTOV, I. C., COGNET, V., SHIDHORE, T. C. & STONE, H. A. 2018 Flow rate–pressure drop relation for deformable shallow microfluidic channels. *J. Fluid Mech.* **841**, 267–286.

CONRAD, W. A. 1969 Pressure–flow relationships in collapsible tubes. *IEEE Trans. Biomed. Engng* **16** (4), 284–295.

DENDUKURI, D., GU, S. S., PREGIBON, D. C., HATTON, T. A. & DOYLE, P. S. 2007 Stop-flow lithography in a microfluidic device. *Lab on a Chip* **7** (7), 818–828.

DUPRAT, C. & STONE, H. A. (Eds) 2016 Fluid–structure interactions in low-Reynolds-number flows. In *Soft Matter Series*. The Royal Society of Chemistry.

EL-ALI, J., SORGER, P. K. & JENSEN, K. F. 2006 Cells on chips. *Nature* **442** (7101), 403.

ELBAZ, S. B. & GAT, A. D. 2014 Dynamics of viscous liquid within a closed elastic cylinder subject to external forces with application to soft robotics. *J. Fluid Mech.* **758**, 221–237.

ELBAZ, S. B. & GAT, A. D. 2016 Axial creeping flow in the gap between a rigid cylinder and a concentric elastic tube. *J. Fluid Mech.* **806**, 580–602.

ELBAZ, S. B., JACOB, H. & GAT, A. D. 2018 Transient gas flow in elastic microchannels. *J. Fluid Mech.* **846**, 460–481.

FUNG, Y.-C. 1993*a* *Biomechanics: Circulation*. Springer.

FUNG, Y.-C. 1993*b* *Biomechanics: Mechanical Properties of Living Tissues*. Springer.

FUNG, Y.-C. 1993*c* *Biomechanics: Motion, Flow, Stress, and Growth*. Springer.

GERVAIS, T., EL-ALI, J., GÜNTHER, A. & JENSEN, K. F. 2006 Flow-induced deformation of shallow microfluidic channels. *Lab on a Chip* **6** (4), 500–507.

GOLDSMITH, H. L. & SKALAK, R. 1975 Hemodynamics. *Annu. Rev. Fluid Mech.* **7** (1), 213–247.

GROTBERG, J. B. 1994 Pulmonary flow and transport phenomena. *Annu. Rev. Fluid Mech.* **26** (1), 529–571.

GROTBERG, J. B. 2001 Respiratory fluid mechanics and transport processes. *Annu. Rev. Fluid Mech.* **3** (1), 421–457.

https://doi.org/10.1017/jfm.2019.994 Published online by Cambridge University Press

GROTBERG, J. B. & JENSEN, O. E. 2004 Biofluid mechanics in flexible tubes. *Annu. Rev. Fluid Mech.* **36**, 121–147.

HAPPEL, J. & BRENNER, H. 2012 *Low Reynolds Number Hydrodynamics: With Special Applications to Particulate Media*. Springer Science & Business Media.

HARDY, B. S., UECHI, K., ZHEN, J. & KAVEHPOUR, H. P. 2009 The deformation of flexible PDMS microchannels under a pressure driven flow. *Lab on a Chip* **9** (7), 935–938.

HEIL, M. 1997 Stokes flow in collapsible tubes: computation and experiment. *J. Fluid Mech.* **353**, 285–312.

HEIL, M. & HAZEL, A. L. 2011 Fluid–structure interaction in internal physiological flows. *Annu. Rev. Fluid Mech.* **43**, 141–162.

HEIL, M., JENSEN, O. E., PEDLEY, T. J. & CARPENTER, P. W. 2003 Flow in collapsible tubes and past other highly compliant boundaries. In *Proceedings of the IUTAM Symposium held at the University of Warwick, United Kingdom, 26–30 March 2001* (ed. P. W. Carpenter & T. J. Pedley). Springer.

HEIL, M. & PEDLEY, T. J. 1995 Large axisymmetric deformation of a cylindrical shell conveying a viscous flow. *J. Fluids Struct.* **9** (3), 237–256.

HOWELL, P., KOZYREFF, G. & OCKENDON, J. 2009 *Applied Solid Mechanics*. Cambridge University Press.

HUPPERT, H. E. 1982 The propagation of two-dimensional and axisymmetric viscous gravity currents over a rigid horizontal surface. *J. Fluid Mech.* **121**, 43–58.

ILIEVSKI, F., MAZZEO, A. D., SHEPHERD, R. F., CHEN, X. & WHITESIDES, G. M. 2011 Soft robotics for chemists. *Angew. Chem. Intl Ed. Engl.* **123** (8), 1930–1935.

JUEL, A., PIHLER-PUZOVIĆ, D. & HEIL, M. 2018 Instabilities in blistering. *Annu. Rev. Fluid Mech.* **50**, 691–714.

KERR, A. D. 1964 Elastic and viscoelastic foundation models. *J. Appl. Mech.* **31** (3), 491–498.

LASHERAS, J. C. 2007 The biomechanics of arterial aneurysms. *Annu. Rev. Fluid Mech.* **39**, 293–319.

LAUGA, E. 2016 Bacterial hydrodynamics. *Annu. Rev. Fluid Mech.* **48**, 105–130.

LISTER, J. R., PENG, G. G. & NEUFELD, J. A. 2013 Viscous control of peeling an elastic sheet by bending and pulling. *Phy. Rev. Lett.* **111** (15), 154501.

LOVE, A. E. H. 1888 The small free vibrations and deformation of a thin elastic shell. *Phil. Trans. R. Soc. Lond.* A **179**, 491–546.

MAJIDI, C. 2014 Soft robotics: a perspective – current trends and prospects for the future. *Soft Robot.* **1** (1), 5–11.

OZSUN, O., YAKHOT, V. & EKINCI, K. L. 2013 Non-invasive measurement of the pressure distribution in a deformable micro-channel. *J. Fluid Mech.* **734**, R1.

PAÏDOUSSIS, M. P., PRICE, S. J. & DE LANGRE, E. 2010 *Fluid–Structure Interactions: Cross-Flow-Induced Instabilities*. Cambridge University Press.

PANDA, P., YUET, K. P., DENDUKURI, D., HATTON, T. A. & DOYLE, P. S. 2009 Temporal response of an initially deflected PDMS channel. *New J. Phys.* **11** (11), 115001.

PATTLE, R. E. 1959 Diffusion from an instantaneous point source with a concentration-dependent coefficient. *Q. J. Mech. Appl. Maths* **12** (4), 407–409.

PEDLEY, T. J. 1980 *The Fluid Mechanics of Large Blood Vessels*. Cambridge University Press.

PEDLEY, T. J. & LUO, X. Y. 1998 Modelling flow and oscillations in collapsible tubes. *Theor. Comput. Fluid Dyn.* **10** (1–4), 277–294.

POLYGERINOS, P., CORRELL, N., MORIN, S. A., MOSADEGH, B., ONAL, C. D., PETERSEN, K., CIANCHETTI, M., TOLLEY, M. T. & SHEPHERD, R. F. 2017 Soft robotics: review of fluid-driven intrinsically soft devices; manufacturing, sensing, control, and applications in human–robot interaction. *Adv. Engng Mater.* **19** (12), 1700016.

POPEL, A. S. & JOHNSON, P. C. 2005 Microcirculation and hemorheology. *Annu. Rev. Fluid Mech.* **37**, 43–69.

RAJ, A. & SEN, A. K. 2016 Flow-induced deformation of compliant microchannels and its effect on pressure–flow characteristics. *Microfluid. Nanofluid.* **20** (2), 31.

RAJ, M. K., DASGUPTA, S. & CHAKRABORTY, S. 2017 Hydrodynamics in deformable microchannels. *Microfluid. Nanofluid.* **21** (4), 70.

https://doi.org/10.1017/jfm.2019.994 Published online by Cambridge University Press

RIVERO-RODRÍGUEZ, J. & SCHEID, B. 2018 Bubble dynamics in microchannels: inertial and capillary migration forces. *J. Fluid Mech.* **842**, 215–247.

RIVERO-RODRIGUEZ, J. & SCHEID, B. 2019 Mass transfer around bubbles flowing in cylindrical microchannels. *J. Fluid Mech.* **869**, 110–142.

RODRÍGUEZ-RODRÍGUEZ, J., SEVILLA, A., MARTÍNEZ-BAZÁN, C. & GORDILLO, J. M. 2015 Generation of microbubbles with applications to industry and medicine. *Annu. Rev. Fluid Mech.* **47**, 405–429.

RUS, D. & TOLLEY, M. T. 2015 Design, fabrication and control of soft robots. *Nature* **521** (7553), 467.

SACKMANN, E. K., FULTON, A. L. & BEEBE, D. J. 2014 The present and future role of microfluidics in biomedical research. *Nature* **507** (7491), 181.

SECOMB, T. W., HSU, R. & PRIES, A. R. 2002 Blood flow and red blood cell deformation in nonuniform capillaries: effects of the endothelial surface layer. *Microcirculation* **9** (3), 189–196.

SEKER, E., LESLIE, D. C., HAJ-HARIRI, H., LANDERS, J. P., UTZ, M. & BEGLEY, M. R. 2009 Nonlinear pressure–flow relationships for passive microfluidic valves. *Lab on a Chip* **9** (18), 2691–2697.

SFORZA, D. M., PUTMAN, C. M. & CEBRAL, J. R. 2009 Hemodynamics of cerebral aneurysms. *Annu. Rev. Fluid Mech.* **41**, 91–107.

SHAPIRO, A. H. 1977 Steady flow in collapsible tubes. *Trans. ASME: J. Biomech. Engng* **99** (3), 126–147.

SHEPHERD, R. F., ILIEVSKI, F., CHOI, W., MORIN, S. A., STOKES, A. A., MAZZEO, A. D., CHEN, X., WANG, M. & WHITESIDES, G. M. 2011 Multigait soft robot. *Proc. Natl Acad. Sci. USA* **108** (51), 20400–20403.

SHIDHORE, T. C. & CHRISTOV, I. C. 2018 Static response of deformable microchannels: a comparative modelling study. *J. Phys.: Condens. Matter* **30** (5), 054002.

SQUIRES, T. M. & QUAKE, S. R. 2005 Microfluidics: fluid physics at the nanoliter scale. *Rev. Mod. Phys.* **77** (3), 977.

STONE, H. A., STROOCK, A. D. & AJDARI, A. 2004 Engineering flows in small devices: microfluidics toward a lab-on-a-chip. *Annu. Rev. Fluid Mech.* **36**, 381–411.

TABELING, P. 2005 *Introduction to Microfluidics*. Oxford University Press.

TAYLOR, C. A. & DRANEY, M. T. 2004 Experimental and computational methods in cardiovascular fluid mechanics. *Annu. Rev. Fluid Mech.* **36**, 197–231.

WEIBEL, D. B., SIEGEL, A. C., LEE, A., GEORGE, A. H. & WHITESIDES, G. M. 2007 Pumping fluids in microfluidic systems using the elastic deformation of poly(dimethylsiloxane). *Lab on a Chip* **7** (12), 1832–1836.

WHITESIDES, G. M. 2006 The origins and the future of microfluidics. *Nature* **442** (7101), 368–373.

XIA, Y. & WHITESIDES, G. M. 1998 Soft lithography. *Angew. Chem. Intl Ed. Engl.* **37** (5), 550–575.

https://doi.org/10.1017/jfm.2019.994 Published online by Cambridge University Press